Ceramics International 51 (2025) 17728–17743

Contents lists available at ScienceDirect

Ceramics International

journal homepage: www.elsevier.com/locate/ceramint

Impact of nickel substitution on supercapacitor and photocatalytic performances of cobalt-ferrites nanoparticles

Dana Toloman [a], Maria Stefan [a], Cameliu Himcinschi [b], Iolanda Ganea [a], Lucian Barbu [a], Arpad Rostas [a], Ahmet Gungor [c], Emre Erdem [c], Adriana Popa [a,*]

[a] National Institute for Research and Development of Isotopic and Molecular Technologies, Donath 67-103, Cluj-Napoca, 400293, Romania
[b] TU Bergakademie Freiberg, Institute of Theoretical Physics, Freiberg, D-09596, Germany
[c] Faculty of Engineering and Natural Sciences, Sabanci University, Tuzla, Istanbul, 34956, Turkey

ARTICLE INFO

Handling Editor: Dr P. Vincenzini

Keywords:
Ni-substituted Co-ferrite
PVDF membrane
Photocatalysis
Supercapacitors

ABSTRACT

$Ni_xCo_{1-x}Fe_2O_4$ nanoparticles were synthesized by precipitation method and developed as bifunctional nanoparticles for photocatalytic and supercapacitor applications. The crystalline structure and gradual changing of the cell parameters by substituting Ni^{2+} ions into the Co-ferrite lattice were confirmed by XRD. Raman analysis shows that the Co^{2+} ions partially substitute Fe^{3+} ions in tetrahedral sites, and the substitution with Ni^{2+} ions lead to a rearrangement of cations on octahedral sites. The samples have a mixture of spherical and rectangular shapes with an average size between 4 and 14 nm for Ni-ferrite and Co-ferrite, respectively. All the samples are ferromagnetic at room temperature; both magnetic phases were evidenced by EPR spectroscopy. In substituted Co ferrite, 80 % Ni was identified as the optimum amount, ensuring the best photocatalytic activity against RhB solution under visible irradiation. The photocatalytic mechanism was explained, considering that the samples generate only superoxide radicals under visible light. The sample with the best photocatalytic performance was combined with PVDF membrane to enhance its hydrophilicity and self-cleaning properties. Additionally, Ni-Co ferrite nanoparticles were studied as electrode materials in symmetrical supercapacitor devices. Electrochemical characteristics indicate good performance and cycling stability and confirmed an appreciable increase in specific capacitance by substituting Co^{2+} with Ni^{2+} ions.

1. Introduction

The rapid development of the economy has led to different environmental issues, which caused serious threats to the long-term development of human society [1]. Releasing toxic compounds like dyes, rubber, plastic, aromatic materials, and paper in water leads to health risks for humans [2]. Due to the concern related to the increase in pollution, environmental standards are becoming stricter [3]. Therefore, finding environmentally friendly technologies for environmental remediation and good actions for sustainable clean energy development is crucial. Photocatalysis, an advanced oxidation process that occur on the semiconductor surface, show great application potential in the field of energy and environmental such as generation of hydrogen (H_2) by water splitting (H_2O) [4], producing electric energy using solar energy by means of photoelectrochemical cell [5], photodegradation of organic pollutants [6], reducing the carbon dioxide (CO_2) to fuels [7]. The photocatalysis process can be explained using energy band theory [8]. At absolute zero, the valence band (VB) is completely occupied with electrons; when the semiconductor is excited with energy higher or equal with the band gap energy (E_g), the photogenerated electrons jump from the VB of the semiconductor to the conduction band (CB), leaving holes in the VB [9]. Therefore, photogenerated holes and electrons participate in the redox reaction at the semiconductor surface [10]. For degradation of organic pollutants, holes can oxidize pollutants directly or react with H_2O/OH^- generating hydroxyl radicals ($\bullet OH^-$), while the electrons interact with the adsorbed oxygen (O_2) from the photocatalyst surface, generating superoxide radicals ($\bullet O_2^-$), which can contribute to the degradation of pollutants.

Spinel ferrite nanoparticles are promising materials in photocatalysis due to their narrow band gap energy (1.1–2.3 eV), which can utilize visible light [11]. Ferrite nanoparticles with superparamagnetic behavior can be synthesized by wet chemical method and are chemically stable, and cost-effective. Additionally, it shows ferromagnetism at room temperature, which enables the photocatalyst to be magnetically

* Corresponding author.
E-mail address: adriana.popa@itim-cj.ro (A. Popa).

https://doi.org/10.1016/j.ceramint.2025.01.543
Received 2 December 2024; Received in revised form 28 January 2025; Accepted 28 January 2025
Available online 13 February 2025
0272-8842/© 2025 The Authors. Published by Elsevier Ltd. This is an open access article under the CC BY-NC-ND license (http://creativecommons.org/licenses/by-nc-nd/4.0/).

separated from the pollutant solution. Ferrite nanoparticles' catalytic and magnetic properties are very sensitive to the chemical composition and synthesis parameters [12].

The spinel structure of ferrites AB_2O_4 is cubic, with closely packed O atoms having the octahedral (B) and tetrahedral (A) sites occupied by Fe^{3+} and metal ions (M^{2+}), respectively. This structure is known as a normal spinel structure. Also, Fe^{3+} may occupy the tetrahedral (A) site, and the octahedral (B) sites can be shared by M^{2+} and Fe^{3+} ions. Such structures are named inverse spinel, illustrated as $B(AB)O_4$ [13]. In this structure, the redox pairs Fe^{3+}/Fe^{2+} and M^{3+}/M^{2+} are present, allowing the fast charge transfer via hopping processes between different valence states cations at relatively lower activation energy [14].

$CoFe_2O_4$ and $NiFe_2O_4$ are known as inverse spinel structures, with the tetrahedral A sites occupied by half of the Fe^{3+} cations. In contrast, the B sites are shared by the rest of the Fe^{3+} and Ni^{2+} or Co^{2+} cations [15]. The metals substitution represents a strategy to enhance optical, electrical, magnetic, and photocatalytic properties, which depend on the doping degree and the distribution of ions in the ferrite network [16–18]. By substituting with various metal (Cu, Mg, Eu, Gd, Dy, Nd) ions, an increase in the photocatalytic degradation of organic pollutant was reported in the literature [19–22]. By substitution, defects are generated in the ferrite nanoparticles, which, together with the reduction of the band gap and the size of the nanoparticles, lead to a more efficient separation and a facile transfer of the photogenerated charges. Moreover, the existence of several possible channels for electron self-trapping due to the multivalent oxidation states of Fe and substituting metal ions drive a better separation of the photogenerated electron-hole pairs (e^--h^+) and a higher photocatalytic activity [23].

One of the significant drawbacks of powder-form photocatalysts is their potentially harmful effects, which remain a topic of debate. If not handled properly, these particles can be released into the environment and may interact with living organisms. Their size is comparable to that of biological molecules, like proteins, allowing them to potentially enter the human body. Even low concentrations of 5–50 μg/L can lead to physiological and chromosomal modification, and oxidative stress [24]. Consequently, slurry reactors are not appropriate for extensive photocatalytic applications. This concern highlights the need to immobilize photocatalysts on supports to mitigate these risks [25]. Recently, various inert materials such as glass, ceramics, polymeric and quartz fibers, silica gel, cement, cellulose membranes, etc. have been employed as supports for powder photocatalysts [26].

The integration of photocatalysts with polymeric membranes is referred to as photocatalytic membrane reactors. This innovative configuration combines the functions of photocatalysis and membrane separation within a single device. It holds significant promise for addressing the challenges of separating catalyst particles in demanding systems and recovering them during wastewater treatment. As a result, photocatalytic membrane reactors retain the benefits of photocatalytic technology for degrading high concentrations of persistent organic waste, while also offering advantages such as non-selectivity, rapid reaction rates, and complete degradation [27].

Among polymer membranes, those based on polyvinylidene fluoride (PVDF) have emerged as a promising option for wastewater treatment, thanks to their excellent mechanical strength, effective separation of organic matter—including carbohydrates and proteins—and high resistance to oxidizing agents [28]. However, fouling remains a significant challenge for the large-scale application of membrane technology. The hydrophobic nature of PVDF membranes contributes to fouling on their surface, leading to a marked decrease in permeate flux, a reduced membrane lifespan, and the need for regular cleaning, which in turn increases energy consumption and operational costs [29]. Most standard polymeric membranes struggle to address these fouling issues, particularly for long-term applications. Consequently, many studies have focused on developing photocatalytic membranes with self-cleaning properties. By incorporating suitable photocatalytic materials, these membranes can be engineered to mitigate fouling through photocatalytic degradation processes [30]. Recently, the integration of photocatalytic materials into the membrane matrix has garnered considerable interest due to their cleaning capabilities [31].

Besides their magnetic and photocatalytic properties, the ferrite materials demonstrated low eddy current losses along with high resistivity, impacting the next generation of energy storage devices [32,33]. Between energy storage devices, supercapacitors are very attractive because of their high-power densities, excellent cyclic stability, and fast charging, being an alternative to batteries due to their applications in mobile electronic devices and memory backup systems [34,35]. A study on the supercapacitive behavior of metal ferrite (Co, Ni, Mn, Cu, Zn) was done previously and shows that $CoFe_2O_4$ has the highest specific capacitance [35]. The specific surface area, the mesoporous surface, and the electron hopping between the cations were reported as the main factors influencing the ferrite supercapacitor behavior. By substituting the metal ferrite with various ions, an improved supercapacitor performance was reported due to the enhancement of the electrochemically active sites [36,37].

In the present study, the precipitation method was utilized to prepare the Co ferrite substituted with Ni ions ($Ni_xCo_{1-x}Fe_2O_4$, x = 0, 0.2, 0.4, 0.6, 0.8, and 1), which is a simple and cost-effective process to synthesize metal oxide nanomaterials with a controllable doping process. Therefore, the required quantities of dopants can be inserted into the chemical solution and incorporated into the final product. By substituting Co ferrite with different Ni content was aimed to modulate photocatalytic and electrochemical performances through the variation of cations distribution at octahedral and tetrahedral site position, which is essential in charge transfer processes involved in above applications. Thus, the morpho-structural, optical, and ferromagnetic properties along with photocatalytic and electrochemical properties of the prepared ferrites are presented and discussed. The visible light photocatalytic property of the samples was investigated following the photodegradation of Rhodamine B (RhB), a synthetic solution. By correlating the structural, optical characteristics with the photogenerated reactive oxygen species (ROS) evidenced by Electron Paramagnetic Resonance (EPR) coupled with spin trapping method and scavenger's experiments, the photocatalytic mechanism was proposed. Additionally, the substituted ferrite with the best photocatalytic performance was combined with PVDF membrane to enhance its hydrophilicity and self-cleaning properties. Also, the electrochemical characteristics of Co ferrite substituted with Ni ions samples show their potential to be used in the field of supercapacitor applications.

2. Experimental

2.1. Materials

The nickel-substituted $CoFe_2O_4$ ($Ni_xCo_{1-x}Fe_2O_4$) nanoparticles were synthesized starting from iron nitrate nonahydrate - $Fe(NO_3)_3{\cdot}9H_2O$ (98 % Alfa Aesar), cobalt nitrate hexahydrate ($Co(NO_3)_2{\cdot}6H_2O$ (98 % Alfa Aesar), nickel nitrate hexahydrate - $Ni(NO_3)_2 \times 6H_2O$ (for synthesis Alfa Aesar), sodium hydroxide - NaOH (97 % Alfa Aesar), oleic acid (Merck) and absolute ethanol (p.a., Alpha Aesar). The aqueous solutions were prepared using Milli-Q water by the Direct-Q 3UV system (Millipore, Bedford, MA). All the chemicals used in this research, including the solvents and reagents, were analytical grade and required no additional purification.

2.2. Sample preparation

2.2.1. Nanoparticles synthesis

$Ni_xCo_{1-x}Fe_2O_4$ nanoparticles were obtained following the precipitation reaction. In 100 ml of distilled water, stoichiometric amounts of cobalt nitrate hexahydrate $Co(NO_3)_2 \times 6H_2O$ and separately nickel nitrate hexahydrate $Ni(NO_3)_2 \times 6H_2O$ were dissolved to generate two solutions. Following dissolution, both solutions were mixed and exposed

to another 30 min of ultrasonication until a homogenous mixture was achieved. Subsequently, a brown precipitate was obtained by adding a 2 M NaOH sodium hydroxide solution to this mixture under continuous stirring until pH = 12. After adding 2 ml of oleic acid, the mixture was mixed continuously for an additional hour. After multiple washes with double-distilled water-alcohol (v:v 1:1), the precipitate was dried in an oven at 70 °C for an average of 12 h. Finally, the powder was calcined for 2 h at 600 °C. Scheme 1 depicts schematically the steps involved in synthesizing the $Ni_xCo_{1-x}Fe_2O_4$ nanoparticles. Several samples were developed, each one containing various amounts of Co substituted by Ni, in the following order: $CoFe_2O_4$, $Co_{0.8}Ni_{0.2}Fe_2O_4$, $Co_{0.6}Ni_{0.4}Fe_2O_4$, $Co_{0.4}Ni_{0.6}Fe_2O_4$, $Co_{0.2}Ni_{0.8}Fe_2O_4$, and $NiFe_2O_4$, abbreviated in the following as CF, CF-20%Ni, CF-40%Ni, CF-60%Ni, CF-80%Ni, and NF, respectively.

2.2.2. Membranes preparation

The PVDF membrane was obtained using the phase inversion method starting from 15 % PVDF powder, 5 % polyethylene glycol (PEG-400) as pore formers and N, N-demethylformamide (DMF) as solvent. The hybrid PVDF-CF-80%Ni membrane contains also 3 % CF-80%Ni nanoparticles. The established amounts of PVDF, PEG and DMF were magnetically stirred 24 h at 60 °C until the polymer is completed dispersed. To obtain the hybrid membrane, after polymer dissolution the nanoparticles were blended using a mechanical stirrer until the solution become homogenous. In the following step, the mixture was kept at 60 °C without stirring to eliminate the air bubbles. The degassed mixture was deposited on a substrate using an MSK-AFA-III thin film applicator. Then, a magnetic bar (1.4 T) was kept perpendicular to the surface of membrane to manipulate the CF-Ni80 % nanoparticles towards the surface. The membrane was deep in a coagulation bath to be separated from the substrate.

2.3. Characterization techniques

For ICP-OS analysis, the solid samples were priory exposed to microwave-assisted acid digestion in a Berghof Speedwave Entry microwave equipped with 10 high-pressure TFM™-PTFE-quartz vessels that allowed maximum pressure and temperature of 40 bar and 230 °C, respectively. The digestion procedure involved adding 0.0145 g of each sample into a 1:1 mixture of 37 % HCl and 69 % HNO_3. Afterwards, the microwave protocol followed a four-step heating trend starting from 75 °C to 180 °C. After cooling, the decomposed samples were diluted up to 50 mL with ultrapure water and further analyzed. An inductively coupled plasma-optical emission spectrometer PlasmaQuant 9100 Elite High Resolution ICP-OES equipped with an Echelle double monochromator, a concentric borosilicate nebulizer, a borosilicate glass cyclonic spray chamber and a V Shuttle Torch with 2 mm quartz injector was used to quantify the metal concentrations in the digested samples. The spectrometer was coupled to a Cetac ASX 560 Autosampler with 240 positions. The axial configuration was employed to identify the elements at the following spectral lines: Mn II 257.610 nm and Zn II 206.200 nm. Argon was used for plasma generation and as auxiliary and nebulization gas at a flow rate of 15, 0.50, and 0.60 l/min, respectively. Ultrapure water and 1000 mg/L multi-element standard solution IV were used to prepare the 7 stock solutions for calibrations. All measurements were performed in triplicate and 2 QC standards were selected for the analysis.

A Rigaku-SmartLab automated multipurpose X-ray Diffractometer was used for X-ray diffraction analysis. The X-ray diffractograms were performed using the following parameters 45 kV, 200 mA, using Cu-Kα radiation. The diffraction patterns were recorded in a step-scanning mode with steps of $\Delta\theta = 0.02°$, in the 2θ range 10–80°. The PDXL2 - Integrated X-ray powder diffraction software was used to process the diffractiograms.

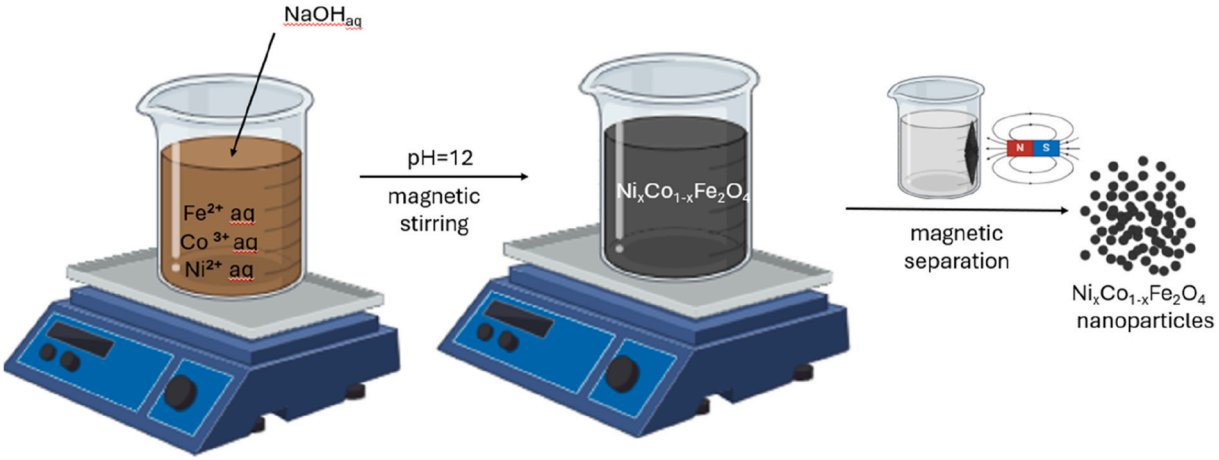
A Micromeritics TriSTAR II 3020 Surface Area and Porosity Analyser was used to evaluate the specific surface area and porosity of decontaminated samples free of moisture or other adsorbents. Adsorption-desorption isotherms were recorded around the boiling point of nitrogen (77 K). Gas pressure was gradually increased until it reached saturation, when the adsorbate (N2) condensed inside the particle pores.

The Raman spectra were measured with a 532 nm excitation from a frequency doubled Nd-YAG laser, at room temperature, using a Labram HR spectrometer equipped with a microscope (50× objective). A 600 mm^{-1} grating was used, and the spectra were collected with an accumulation time of 10 s and 60 repetitions.

Scanning transmission electron microscopy (STEM) was utilized to analyze the morphology of the nanoparticles. The STEM investigation was performed using a Hitachi SU8230 microscope equipped with a cold field emission gun that accelerates the electron at 200 kV.

Electron paramagnetic resonance (EPR) spectroscopy experiments were accomplished on a Bruker E−500 ELEXSYS spectrometer, using Q-band microwave bridge (33.9 GHz) at room temperature: microwave power 1.39 mW, modulation frequency of 100 kHz and X-band (9.52 GHz) in the temperature range between 110 and 500 K under identical conditions: microwave power 0.635 mW, modulation frequency of 100 kHz.

Reflectivity spectra were obtained using a JASCO V570 UV–VIS–NIR Spectrophotometer having an absolute reflectivity measurement JASCO ARN-475 accessory. The absorption spectra were achieved using an internal soft of the spectrometer.



Scheme 1. Illustration of the steps involved in synthesizing $Ni_xCo_{1-x}Fe_2O_4$ nanoparticles.

2.4. Photocatalytic activity evaluation

The photodegradation of the RhB and phenol pollutant was performed using a homemade laboratory-visible-reactor equipped with an ultrasonic bath and a 400 W halogen lamp (Osram). The ferrite nanoparticles (6 mg) were dispersed in a 12 ml pollutant (RhB: 1.0×10^{-5} mol/l, phenol: 0.7×10^{-4} mol/l) solution, and then the obtained solution was stirred in the dark for 60 min to attain the adsorption equilibrium. Each photocatalytic experiment was continuously performed for 300 min. Every 60 min, a part of the resulting solution (3.5 ml) was examined using a UV–Vis spectrophotometer. The photocatalytic activity was evaluated by recording the pollutant-specific maximum absorbance and is calculated using the following equation:

$$\textit{Photocatalytic activity}\ (\%) = \left(1 - \frac{C_t}{C_0}\right) x\ 100 \quad (1)$$

where C_t and C_0 represent the pollutant concentration at time t and time t = 0, respectively. A calibration curves was used to calculate the pollutant concentration corresponding to the measured absorbance (Fig. S1).

2.5. Reactive oxygen species (ROS) evaluation

EPR spectroscopy coupled with the spin-trapping method were used to monitor the ROS generation. As a spin-trapping reagent, 5,5-Dimethyl-1-pyrroline N-oxide (DMPO) was used. The ferrite nanoparticles (10 mg) were mixed in DMSO (1 ml) and dispersed in an ultrasound bath (30 min). Further, DMPO of 0.2 M concentration was appended to the above mixture. The obtained solutions were transferred into the quartz capillary tubes for liquid measurements and subjected to visible irradiation.

2.6. Electrochemical measurements

The electrochemical characteristics were examined utilizing a Biologic VMP300 potentiostat. The electrochemical behavior was assessed using various techniques, including electrochemical impedance spectroscopy (PEIS) under potentiostatic conditions, cyclic voltammetry (CV), and galvanostatic cycling with potential limitation (GCPL). The PEIS investigation utilized a 1M $LiPF_6$ electrolyte with a glass fiber as a separator in a symmetric configuration, employing a frequency range ranging from 10 mHz to 1 MHz. The investigation of the CV was conducted using a scan rate range of 1–200 mV/s, with an applied voltage window range of 0V–2.5 V. The investigation conducted using the GCPL method involved the examination of supercapacitors that had been designed using Ni-Co ferrite nanoparticles. During this analysis, a range of current densities was applied, spanning from 0.1 A/g to 2.4 A/g. Equation (2) was utilized to evaluate the specific capacitance (C_s). Equations (3) and (4) were employed to calculate the fabricated electrode's energy and power densities, respectively.

$$C_{s,} = \frac{\int_{V_1}^{V_2} I(V)dV}{2mv\Delta V} \quad (2)$$

$$\textit{Energy Density}, E = \frac{0.5 * C_s * \Delta V^2}{3.6} \quad (3)$$

$$\textit{Power Density}, P = \frac{E}{(\Delta t/3600)} \quad (4)$$

where, Cs represents the specific capacitance in Farads per gram (F/g), ΔV denotes the maximum potential window in volts (V), E represents the energy density, and Δt signifies the discharge period.

3. Results and discussions

3.1. Elemental, structural and morphological characterization

ICP-OES analysis was performed to verify the elemental composition of the samples. The molar concentration of the cations presents in the sample is displayed in Table 1. The molar percentage of Ni was evaluated as the ratio between the molar concentration of Ni and the sum of Ni and Co molar concentrations, and the obtained values follow the ratios established in the synthesis.

Structural information about the crystalline phases was obtained by X-ray diffraction, and the diffractograms are presented in Fig. 1a.

All diffraction patterns are indexed in the Fd3m space group with cubic symmetry (DB card No. 01-077-9720) without any trace of impurity. Increasing the Ni content broadens the diffraction peaks, meaning that the mean crystallite sizes decrease with the increase in the Ni content. To identify the influence of the Ni content on the lattice structure of $CoFe_2O_4$, cell parameters, unit cell volume, and crystallite mean sizes were calculated using the Rietveld refinement and Williamson-hall method, respectively. The obtained values are summarized in Table 2.

As can be observed from Table 2, the cell parameter and, consequently, the unit cell volume are smaller compared with the corresponding one for CF. Excepting the CF-40%Ni, a linear decrease of the cell volume with the increase of Ni concentration is observed. The cell volume decrease was expected since the ionic radius of Ni^{2+} (0.69 Å) is smaller than Co^{2+} (0.74 Å). The small increase of the CF-40%Ni cell volume can probably be due to the redistribution of Ni cations between the tetrahedral and octahedral sites of the spinel structure, taking into account that the size of the octahedral B-site is larger than the size of the tetrahedral A-site, [38,39]. The crystallite's mean size dimensions, D, decrease by increasing the Ni content, from 14 nm for $CoFe_2O_4$ to 4 nm for $NiFe_2O_4$. Similar behavior was previously reported and attributed to the smaller radius of the ion replacing the cations in the ferrite [40].

Additional structural information was obtained by Raman spectroscopy. In Fig. 1b are shown the Raman spectra of the investigated samples to obtain more information about the microstructure variation. As was stated above, the crystalline structure of Ni-Co ferrites belongs to cubic symmetry, and the theoretical analysis predicts five active optical modes in Raman, known as A_{1g}, E_g and three T_{2g} [41–43]. The differences between these modes are due to the motion of oxygen in both tetrahedral and octahedral sites [44]. The Raman spectrum of Co-ferrite consists of four bands. The first one at 677 cm^{-1} was assigned to the $A_{1g}(1)$ mode characteristic to the symmetric stretching vibrations of oxygen atoms along metal ions located in tetrahedral sites, and one band at 600 cm^{-1} was assigned to the $A_{1g}(2)$ mode representing the stretching vibration of Fe–O in the tetrahedral site. The presence of both modes, $A_{1g}(1)$ and $A_{1g}(2)$, means that Co^{2+} ions partially substitute Fe^{3+} ions in tetrahedral sites [45]. The two bands at 468 cm^{-1} and 198 cm^{-1} were attributed to the $T_{2g}(2)$ and $T_{2g}(3)$ modes, respectively, and one band at 317 cm^{-1} was assigned to E_g mode. These bands are the results of the symmetric and anti-symmetric bending of oxygen atom with metal ions (M − O) at octahedral sites [46,47].

A systematic shift of band position can be observed by substituting Co^{2+} ions with Ni^{2+}, and by increasing the Ni content. The band due to

Table 1
Samples composition as determined from ICP-OES.

Sample	C_{Ni} (mmol/L)	C_{Co} (mmol/L)	C_{Fe} (mmol/L)	C_{Ni} (mol %)
CF	0.000	0.920	1.416	0
CF-20%Ni	0.077	0.267	1.235	22
CF-40%Ni	0.390	0.526	1.940	43
CF-60%Ni	0.648	0.390	2.195	62
CF-80%Ni	0.667	0.166	1.940	80
NF	0.908	0.000	1.912	90

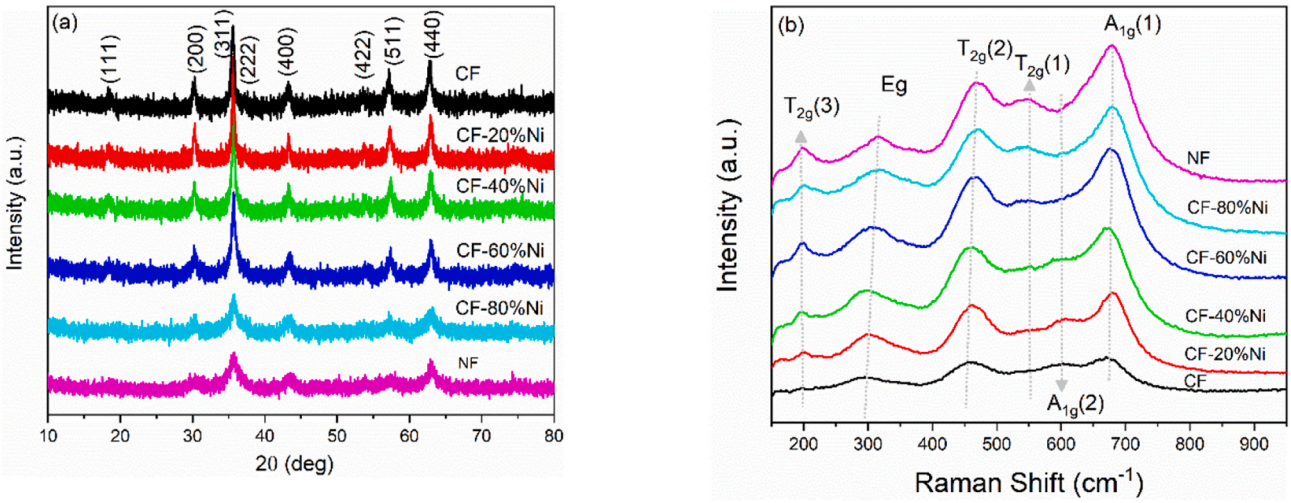


Fig. 1. X-ray diffraction patterns of the $Ni_xCo_{1-x}Fe_2O_4$ nanoparticles (a) and Raman spectra of the $Ni_xCo_{1-x}Fe_2O_4$ nanoparticles (b).

Table 2
Cell parameters, unit cell volume, and crystallite mean sizes of the samples.

Sample	a (Å)	b (Å)	c (Å)	V (Å^3)	D (nm)
CF	8.3663	8.3663	8.3663	585.60	14 ± 0.5
CF-20%Ni	8.3523	8.3523	8.3523	582.66	10 ± 0.5
CF-40%Ni	8.3562	8.3562	8.3562	583.49	12 ± 0.7
CF-60%Ni	8.3493	8.3493	8.3493	582.03	10 ± 0.3
CF-80%Ni	8.3492	8.3492	8.3492	581.81	6 ± 0.2
NF	8.3335	8.3335	8.3335	578.75	4 ± 0.2

$A_{1g}(2)$ is decreasing and disappears, and two new bands are better resolved one at 550 cm^{-1} attributed to $T_{2g}(1)$, and the other one at 200 cm^{-1} assigned to $T_{2g}(3)$. The changes in bands position and intensity with increasing Ni content are probably due to a rearrangement of the cations on octahedral sites.

The sample's morphology was analyzed by TEM, and the images corresponding to CF, CF-80%Ni, and NF nanoparticles are illustrated in Fig. 2.

Fig. 2a, corresponding to the CF sample, comprises dispersed particles having a mean size dimension of 14 nm, and the nanoparticle shape is mainly rectangular. The CF-80%Ni nanoparticles (see Fig. 2b) have a spherical and rectangular shape with a mean size dimension of 7 nm. The NF sample (Fig. 2c) reveals the presence of agglomerated small nanoparticles. The mean size of these nanoparticles is 4 nm. The nanoparticles' magnetic nature can explain the nanoparticle's agglomeration tendency. The nanoparticle sizes follow the crystallite sizes estimated by XRD.

3.2. Electron Paramagnetic Resonance (EPR) characterization

Information about the magnetic behavior of the compounds can be obtained from EPR spectroscopy. The EPR spectra measured in Q-band at room temperature of all the samples are exhibited in Fig. 3a. The EPR experimental parameters are presented in Table 3. By increasing the Ni content, the resonance field (H_R) is shifted to a higher magnetic field, and the internal field (H_{int}) and the linewidth (ΔH_{pp}) decrease. The internal field represents the sum between the internal magnetic field due to demagnetization, dipole–dipole interaction between the neighboring magnetic nanoparticles, and dipole–dipole interaction between agglomerates and was evaluated based on previous studies [48–50].

Co-ferrite nanoparticles show an asymmetric resonance signal reflecting dipolar interaction and to the anisotropic nature of cobalt ions driving to strong surface anisotropy [51,52]. The asymmetry is due to arbitrary orientation of the magnetic moments having various directions of the anisotropy axes [48]. By substituting the Co^{2+} ions with Ni^{2+} ions, the resonance signal becomes narrow due to the superexchange interaction between magnetic moments. The resonance field H_R linearly increases due to the substitution with Ni^{2+} ions. The presence of Ni^{2+} ions cause a decrease in the magnetic moment, which decreases the total magnetic moment following a decrease in the internal fields [49]. All the samples are ferromagnetic at room temperature so that they can be easily manipulated in solution.

The ferromagnetic behavior of the samples was investigated in X-band in the temperature range 110–500 K. For example, Fig. 3b illustrates the EPR spectra of CF, NF, and CF-60%Ni at 230 K. The EPR signal of Co-ferrite is well resolved, only starting at 250 K. At this temperature, the EPR signal of CF-60%Ni clearly shows the contribution of both ferrites, attesting the presence of both phases $CoFe_2O_4$ and $NiFe_2O_4$ in the nanomaterial. The presence of both phases is sustained by the behavior of the resonance field, H_R, in the studied temperature range. Fig. 3c exhibits the temperature dependence of H_R for all samples. It can be observed that the resonance field of the substituted ferrite samples in

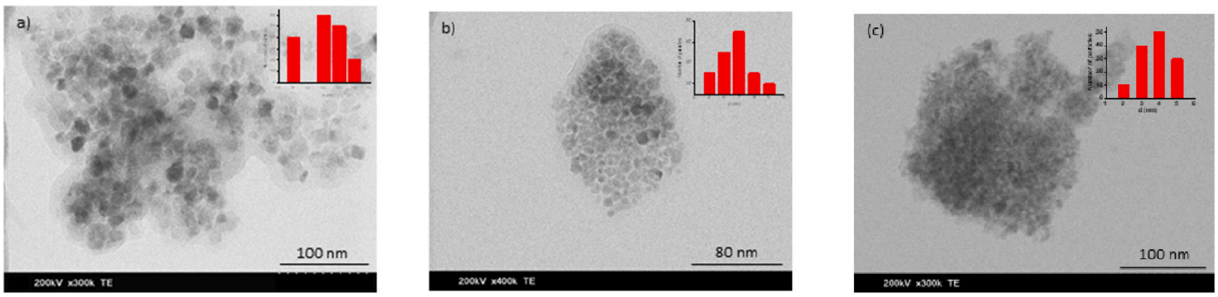


Fig. 2. TEM images of (a) $CoFe_2O_4$, (b) CF-80%Ni and (c) $NiFe_2O_4$, together with their corresponding sizes distribution.

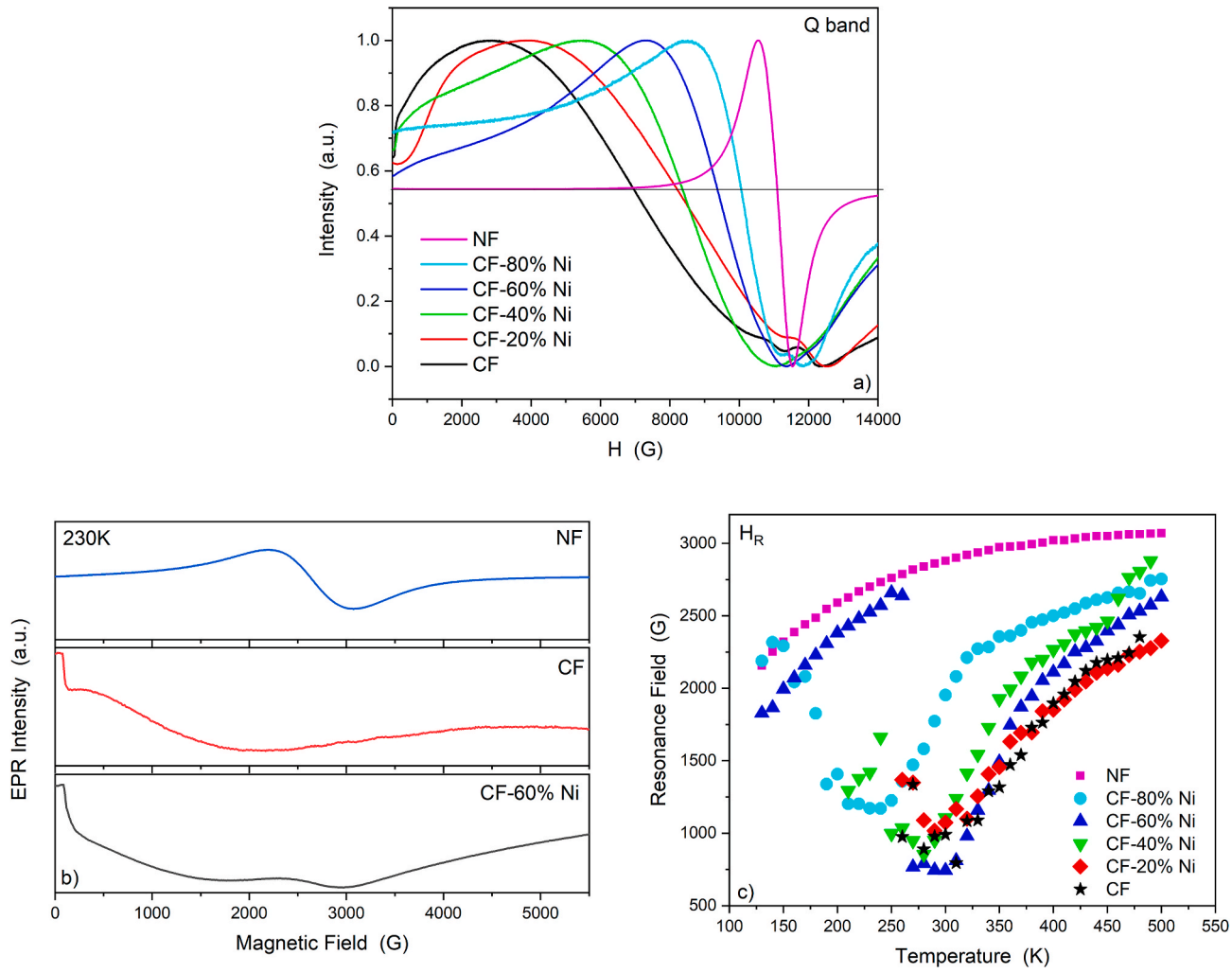


Fig. 3. EPR spectra of all the samples in Q-band (35,5 GHz) at room temperature (a); FMR spectra of CF, NF, and CF-60%Ni at 230K (b). Temperature dependence of HR for all samples (c).

Table 3
Resonance field H_R, internal field H_{int}, and the linewidth ΔH_{pp} of the samples.

Sample	H_R (G)	H_{int} (G)	ΔH_{pp} (G)
CF	6987	5133	9735
CF-20%Ni	8232	3888	8703
CF-40%Ni	8363	3757	5500
CF-60%Ni	9368	2752	4044
CF-80%Ni	10058	2062	3247
NF	11089	1031	1016

function of the temperature follows the behavior of the components being between them, but much closer to Co-ferrite, excepting the CF-60%Ni sample whose behavior at lower temperature (T < 250 K) is much closer to the NF sample.

3.3. Optical properties

The samples optical response was investigated using UV–Vis spectroscopy. The UV–Vis absorption spectra exhibited in Fig. 4a show that the samples possess excellent visible light response. Besides, Ni-ferrite has an intense band centered at 745 nm due to the d-d transition from Ni (3d-t_{2g}) to Ni (3d-e_g) [53].

By substituting Co-ferrite with Ni ions and increasing the Ni content, the absorption edge shows a gradual blue shift due to the decrease in nanoparticle size [54]. Using absorption spectra and applying Tauc's law, the samples band gap energy was determined, and the obtained values are inserted in the inset of Fig. 4b [55]. Increasing the Ni content increases the band gap energy from 1.12 eV for $CoFe_2O_4$ to 1.40 eV for $NiFe_2O_4$. The decrease in the band gap energy may be due to the ionic radii of Ni^{2+} ions which is smaller than Co^{2+} ions generating deeper Ni^{2+} states due to the strong electrostatic interaction. The difference between $CoFe_2O_4$ and $NiFe_2O_4$ is that in the first case the Co states are localized at the valence band edge and in the case of Ni-ferrite, Ni states are more hybridized [56,57].

3.4. Photocatalytic activity

The photocatalytic activity of Ni-substituted $CoFe_2O_4$ nanoparticles was assessed by RhB degradation under visible light irradiation. The irradiation was performed after the adsorption-desorption balance was reached. The equilibrium between the catalyst and RhB dye was attained after 60 min of the absorption process. In Fig. 5a, the RhB removal rates of the prepared samples are presented comparatively. The figure also contains the RhB solution photolysis. As can be observed, no important self-degradation was obtained. It can be observed that the samples show different adsorption abilities. The $NiFe_2O_4$ nanoparticles have the highest adsorption capacity, 37 %, followed by CF-80 % Ni and CF-40 % Ni. These results are in accordance with the specific surface area obtained from BET measurements (Fig. S2) and can be a consequence of

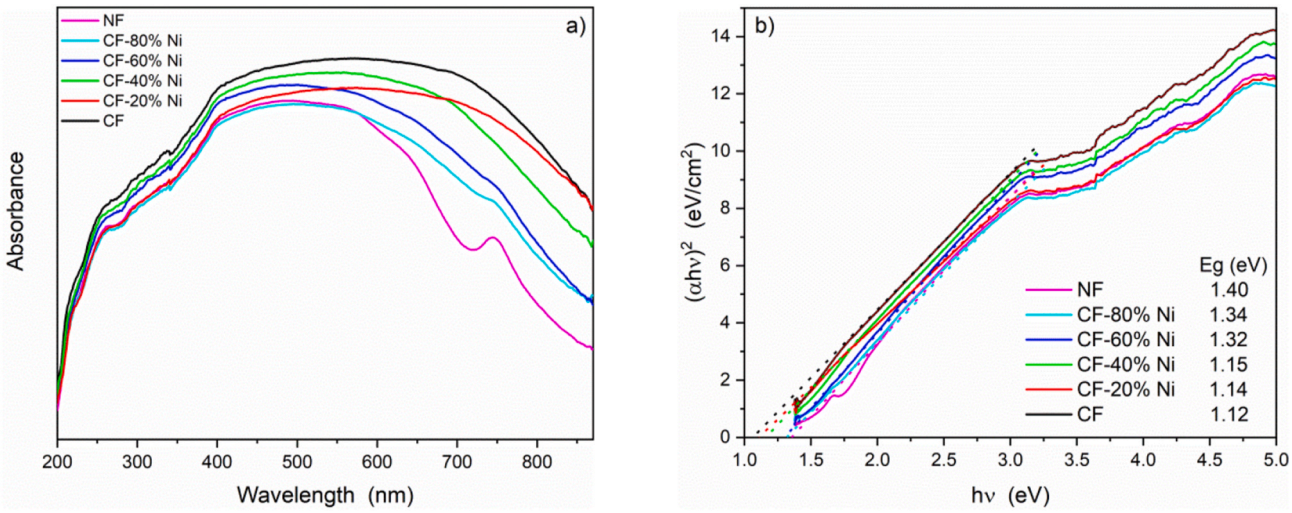


Fig. 4. UV–Vis absorption spectra (a). Tauc's plots (b).

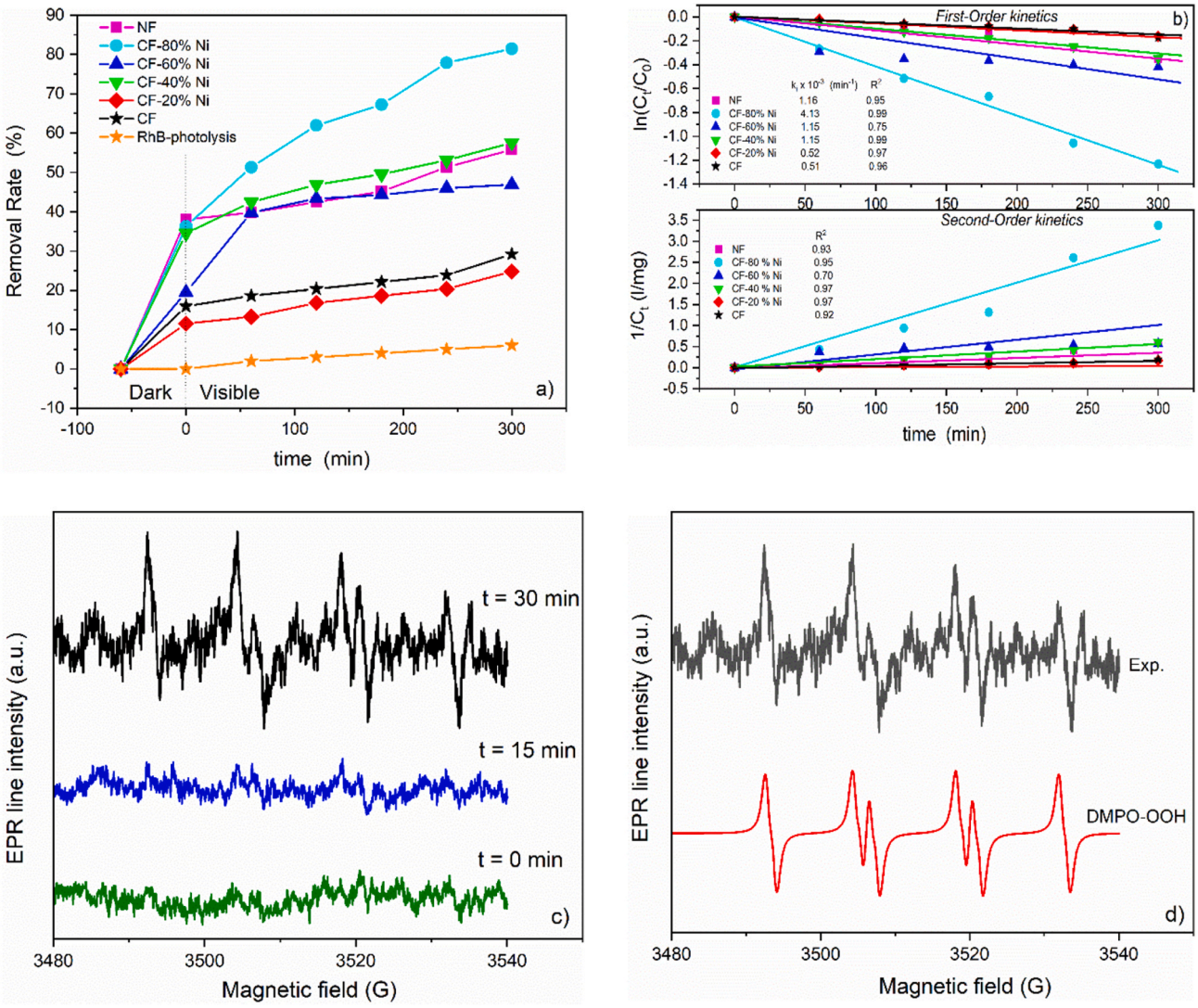


Fig. 5. The removal rate of the samples (a). The RhB degradation kinetics (b). Experimental spectra of DMPO spin adducts generated by CF-80%Ni sample under different irradiation periods (c). Experimental and simulated spectra of DMPO spin adducts generated by the CF-20 % Ni sample under 30 min visible light irradiation (d).

the smaller sizes of these nanoparticles compared to that of $CoFe_2O_4$, CF-20 % Ni, and CF-60 % Ni. A large surface area assures a higher contact with the pollutant molecules.

The highest removal rate of 81 % was obtained for the CF-80 % Ni sample and decreased with the further decrease of Ni content. To illustrate the kinetic mechanism for the degradation of RhB pollutant in the solution the pseudo-first order (Eq. (5)) and pseudo-second order kinetics (Eq. (6)) models were applied:

$$\ln (C_t / C_{0)} = -k_1 \bullet t \quad (5)$$

$$\frac{1}{C_t} - \frac{1}{C_0} = k_2 \bullet t \quad (6)$$

where C_0 and C_t are the initial concentration and concentration after time t; k_1 and k_2, are the rate constants of first-order and second-order equation, respectively. To calculate the concentration C_t, the calibration curve was used. The fits with the pseudo-first-order and second-order equation are presented in Fig. 5b. The obtained correlation coefficients (R^2) after the fits suggest that the pseudo-first-order kinetic model describes the photocatalytic process. The kinetic constant (k_1) was evaluated from the fitted curves' slope with the pseudo-first order kinetic model. The obtained values are presented in the inset of Fig. 5b, which sustains the observation that CF-80 % Ni has the highest photocatalytic activity. The photocatalytic activity decreases in the following order: CF-80%Ni > NF > CF-60%Ni > CF-40%Ni > CF-20%Ni > CF. Consequently, 80 % Ni represents the optimum content, assuring the best RhB removal rate.

To rule out the possibility of photosensitization, the CF-80 % Ni sample was also tested for phenol degradation, a colorless pollutant. The evaluation of both adsorption capacity and photocatalytic activity followed the same protocol used for the RhB solution, with the UV–Vis absorbance of phenol's specific band at 269 nm being monitored. The results are presented in Fig. S3. Photolysis of the phenol solution showed no significant self-degradation. The adsorption–desorption equilibrium was achieved within 60 min, with the sample showing an adsorption rate of approximately 26 %. After 5 h of visible light irradiation, the removal rate reached 79 %, corresponding to a photocatalytic rate constant of $k_i = 4.59 \times 10^{-3}$ min^{-1}.

EPR spectroscopy coupled with the spin-trapping technique was applied to detect and quantify the generated ROS species. The EPR measurements were performed on the CF-80 % Ni sample, which exhibited the best photocatalytic activity. Before irradiation, no EPR spectrum was obtained, but by increasing the irradiation time, a 6-line spectrum was acquired (Fig. 5c).

A simulation was used to determine the formed spin-adducts. Fig. 5d illustrates the spectrum obtained after 30 min of irradiation and its simulation. The Hamiltonian parameters resulting after EPR spectra simulation confirm the generation of the: •DMPO-OOH ($a_N = 13.8$ G, $a_H^{\beta} = 11.8$, $a_H^{\gamma} = 0.9$ G, $g = 2.0098$) spin adducts. The •DMPO–OOH adduct is formed when O_2^- radicals interact with DMPO [58]. Consequently, the O_2^- is the ROS generated by the sample under visible light irradiation. To reveal the active species involved in the photocatalytic degradation of RhB, three scavenger agents were used to block their activity. Vitamin C was selected as scavengers for $O_2^{\bullet -}$, Ethylenediaminetetraacetic Acid (EDTA) for h^+, and Isopropanol for •OH radicals, respectively. The experiment was performed by adding 5 mM quenchers to the initial solution and all conditions were kept identical. The results are presented in Fig. S4 and show a considerable inhibition of the photocatalytic activity when vitamin C is used as quencher suggesting that the $O_2^{\bullet -}$ is involved in the photodegradation process.

Generally, the photocatalytic mechanism can be explained by generating electron-hole pairs when the nanoparticles are excited with visible light higher than the energy band gap. If these pairs are not recombined, they can participate in photo-oxidation and photo-reduction reactions. In the case of our samples, EPR experiments coupled with the spin-trapping technique show that our sample generates only superoxide radical, which means that the potential of valence band position is lower than the oxidation of the OH^-/•OH and H_2O/•OH redox pair; therefore, these reactions cannot happen [59]. Therefore, the photocatalytic process is only due to the superoxide radicals generated by the interaction between electrons and surface-adsorbed O_2. As was stated in the UV–Vis part, Ni ions introduced supplementary levels in the band gap of Co-ferrite, which can act as electron trapping sites, diminishing the faster recombination of electron-hole pairs. Moreover, many redox pairs (Fe^{3+}/Fe^{2+}, Co^{3+}/Co^{2+}, Ni^{3+}/Ni^{2+}) favor the electron transport, increasing the charge transfer to the surface sites [60,61].

To avoid accidental contamination of water with nanoparticles and to use them on a larger scale, we immobilized the photocatalyst on a PVDF polymer membrane. Therefore, the photocatalyst with the best pollutant removal efficiency was embedded in a PVDF membrane and using a magnet the nanoparticles were brought to the surface of the membrane for a better interaction with light and pollutant molecules. In Fig. 6, SEM images of the PVDF, respectively PVDF-CF-80%Ni membranes are shown. As it can be observed in Fig. 6a–d the pores are uniformly distributed at the membrane top side having a mean size of 4 μm. The bottom size of the membrane (Fig. 6b–e) is less porous, having pores of approximately 1 μm in diameter. The cross section (Fig. 6c–f) indicates the formation of an asymmetric structure made up of a succession of layers. The upper part consists in a porous layer having a mean thickness of 80 μm. Between these two parts, parallel pores are formed with diameter varying between 15 and 20 μm. The cross-sectional SEM image reveals that the membrane thickness is approximately 170 μm.

In the case of the PVDF-CF-80%Ni membrane prepared in the presence of a magnetic field (Fig. 6e), nanoparticles agglomerations can be observed on the lower surface of the membrane. They are also visible in the pores of the membrane, as observed in Fig. 6f.

To confirm the nanoparticles presence on the membrane surface an elemental analysis was carried out by EDX. The obtained images are presented in Fig. 7. The presence of fluorine (F) is observed, the main component of the PVDF membrane, respectively of Fe, Ni and O, the constituent elements of the incorporated nanoparticles.

The membranes optical response was studied by UV–VIS spectroscopy. The obtained absorption spectra are illustrated in Fig. 8. An increase of the visible range absorption appeared in the case of the membrane PVDF-CF-80%Ni due to the nanoparticles influence.

An important property of the membrane is its hydrophilicity. A hydrophilic membrane ensures a reduced loading of the membrane with pollutant molecules.

The hydrophilic character was determined by measuring the contact angle between the water molecules and the membrane. The results are presented in Fig. 9. The PVDF membrane have a contact angle of 87 deg. By modifying the membrane with CF-80%Ni nanoparticles, the contact angle is reduced to 65 deg. This increase in the hydrophilicity can be explained by the presence of hydroxyl groups on the nanoparticles surface [62].

The membrane ability to remove the organic pollutant was determined using a RhB synthetic solution under visible light irradiation. Fig. 10 shows the removal rate of PVDF and PVDF-CF-80%Ni membranes after 4h in dark and under visible light irradiation.

In dark, an adsorption process take place, PVDF-CF-80%Ni showing a higher adsorption degree due to the cumulative effect of membrane and nanoparticles. In the case of PVDF membrane the difference between removal rate in dark and under irradiation (~5 %) is due to the photolysis process of RhB. Instead, PVDF-CF-80%Ni membranes show a higher removal rate of 85 % under light irradiation due to the adsorption and photocatalysis processes. The photocatalytic process is sustained by the CF-80%Ni particles from the membrane surface. By photocatalysis, not only the RhB molecules in the solution are degraded, but also the molecules that have been adsorbed on the membrane surface, which

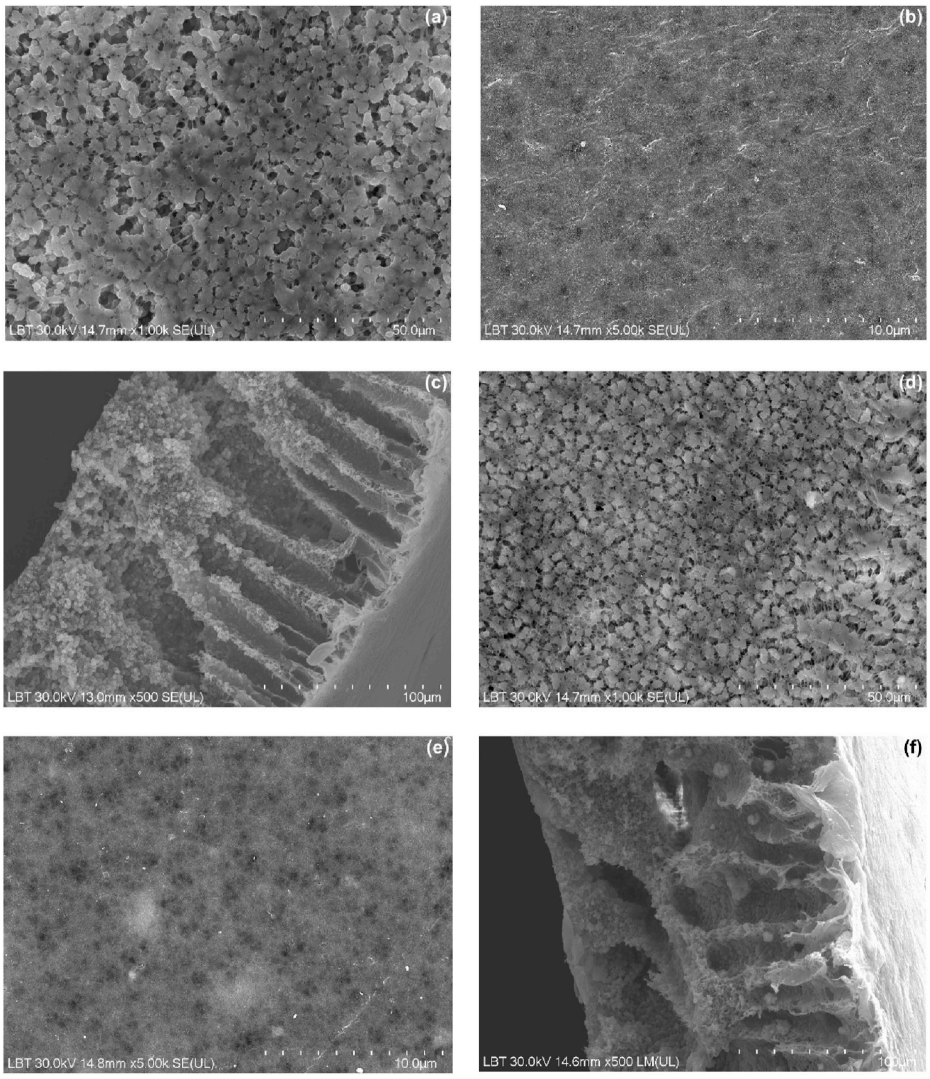


Fig. 6. SEM images of (a,d) top size, (b,e) bottom size, (f) cross section of PVDF and PVDF-CF-80%Ni, respectively.

reduced membrane fouling. As can be observed in Fig. 10 difference in coloration between membranes appears. This is due to the PVDF-CF-80%Ni membrane self-cleaning by photocatalysis.

3.5. Electrochemical performance

The electrodes containing $Ni_xCo_{1-x}Fe_2O_4$ ($0 < x \leq 1$) were assessed for their supercapacitive behavior using CV, electrochemical impedance spectroscopy PEIS, and GCPL tests in a two-electrode configuration. Fig. 11 depicts the cyclic voltammetry characteristics of the $Ni_xCo_{1-x}Fe_2O_4$ ($0 \leq x \leq 1$) electrodes, which were examined at different scan rates spanning from 1 to 200 mV/s. All materials' CV profiles exhibited similar curve patterns when subjected to low and high scanning rates, suggesting similar reversibility and rate capacity [63,64]. Moreover, it is possible to deduce that the electrode exhibits exceptional rate capability and electrochemical reversibility, as indicated by the peak current increase with the scan rate escalation from 1 to 200 mV/s [64]. The charging and discharge phases had a rectangular pattern, characteristic of an Electric Double-Layer Capacitor (EDLC), with no apparent redox peaks [65].

There is a noticeable increase in the area under the CV curve as the concentration of Ni decreases. The maximum value of the area was attained at 20 % Ni content. Therefore, it can be deduced from the cyclic voltammetry (CV) curves that the specific capacitance of the material is influenced by Ni^{2+} substitution. Decreasing the scan rate results in an increase in the area under the CV curve. This observation suggests an elevation in the C_s value. The recorded polarization may be attributable to the increased scan rate caused by the diffusion-controlled process. The CV curves of all samples demonstrate a rapid current response to voltage reversal even at higher scan rates, indicating low equivalent series resistance and acceptable capacitance characteristics [66].

The examination of impedance is a fundamental technique used to evaluate electrochemical systems' effectiveness, investigate the interactions occurring at electrode surfaces, and ascertain the inherent resistance present in the material [67].

The Nyquist curves of each sample are depicted in Fig. 12, along with the fitting analysis conducted for each curve. By substituting Co ions with 20 % Ni in the lattice of $CoFe_2O_4$, the impedance value decreases with an order of magnitude, both for the real and imaginary parts. However, increasing the Ni content leads to a gradual increase. This behavior was expected due to increasing the band gap energy of the samples by increasing Ni content. The electrical resistivity of a material is generally reduced as the band gap energy is decreased, enabling more efficient conducting of electrical current through the free carriers, resulting in increased energy gain.

Table 4 displays the circuit elements that were acquired from the Z-fit analysis. R_1, R_2, and R_3 denote the electrolyte's internal resistance between the electrodes, the electrostatic interaction at the interface

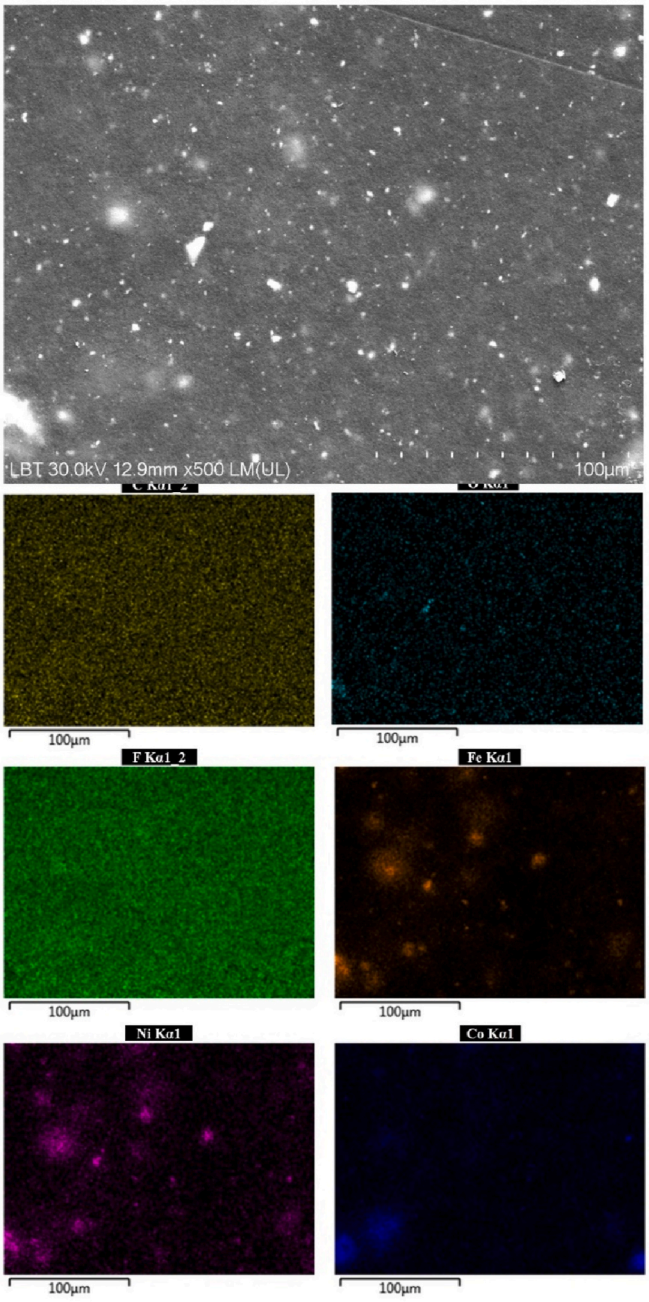


Fig. 7. EDX image and elemental mapping of PVDF-CF-80%Ni membrane.

between the electrode and the solution, and the resistance arising from the semiconductor characteristics of the electrode material, respectively [68].

The variables Q_2 and Q_3 denote the electrode's capacitance and the ions' diffusion-limited behavior in the electrolyte, respectively [67,68]. Upon analysis of the R_1 values, it is evident from Table 4 that CF exhibits an elevated internal resistance, which decreases by Ni substitution in the lattice of Co-ferrite, except the Ni-ferrite. This phenomenon can provide challenges in electron transport to the electrode's surface, impacting the efficiency of electrode reactions, which can be enhanced by fast electron transport, whereas high resistance can impede this process. Inspecting the effect of double-layer resistance (R_2), it is evident that higher resistance characterizes Co-ferrite. Substituting with Ni leads to a reduction in resistance except for CF-40%Ni sample. The reduction in R_2 values with Ni substitution indicates enhanced charge transfer efficiency at the electrode-electrolyte interface. This can be attributed to the

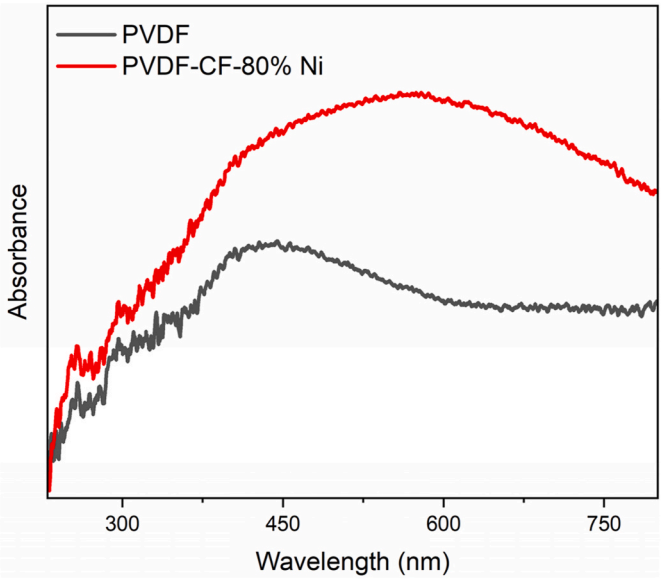


Fig. 8. UV–Vis absorption spectra of PVDF and PVDF-CF-80%Ni membranes.

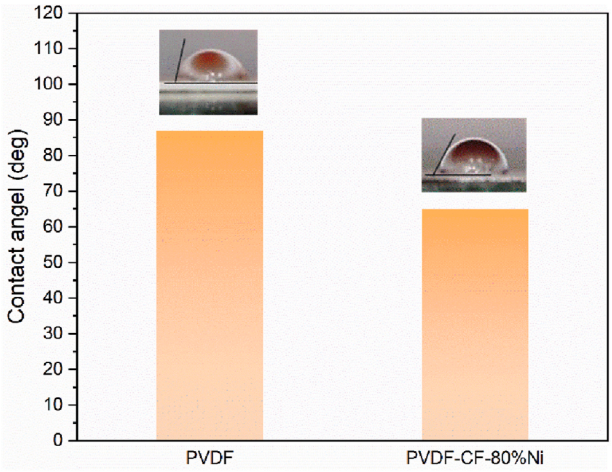


Fig. 9. The contact angle for PVDF and PVDF-CF-80%Ni membranes.

rearrangement of Ni^{2+} ions in octahedral positions, the presence of multiple redox pairs (Fe^{3+}/Fe^{2+}, Co^{3+}/Co^{2+}, Ni^{3+}/Ni^{2+}) which facilitates faster charge transfer. Furthermore, the R_3 value, which characterizes the diffusion-limited performance of ions in the electrolyte, experiences a substantial increase by Ni substitution. Furthermore, based on the research conducted using XRD, it has been seen that, the unit cell volume gradually decreases as the concentration of Ni increases. The increase in R_3 values with Ni substitution reflects the diffusion-limited behavior of ions in the electrolyte. However, the decrease in unit cell volume observed in XRD analysis is expected to positively impact on the ion diffusion rate, partially offsetting this effect. For CF-20%Ni, the low R_3 value indicates faster ion transport to the electrode surface [69]. The Q_2 values are related to the electrode capacitance in the electrolyte, and it is obvious that the addition of Ni to the $CoFe_2O_4$ structure results in an increase of Q_2. This indicates an enhancement in the amount of active material on the electrode surface and the effectiveness of reactions at the electrode-electrolyte interface. The increase in Q_2 values further supports the enhancement in electrode capacitance, while the low band gap energy of CF-20%Ni facilitates faster charge transfer, contributing to its superior electrochemical performance. The increase in Q_3 values reflects the diffusion-limited behavior of ions in the electrolyte.

GCPL investigation was conducted to assess the specific capacities

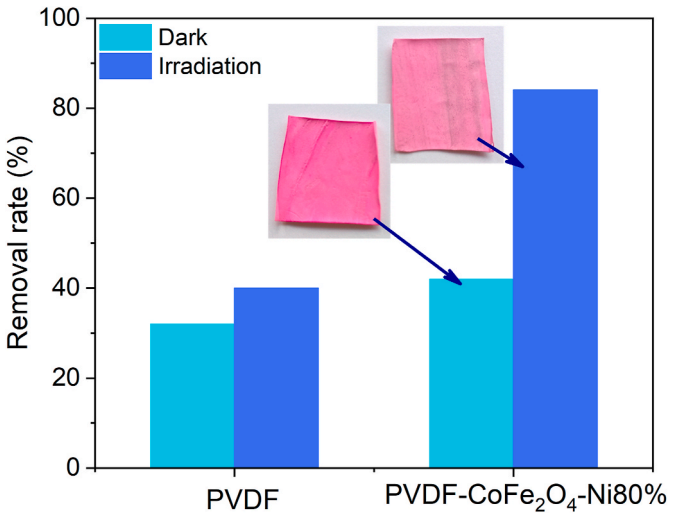


Fig. 10. RhB removal rate in dark and under visible-light irradiation in the presence of prepared membranes. The inset shows the self-cleaning ability of the hybrid membrane.

(mAh/g) of the Ni-Co ferrite nanoparticles. The primary objective was to evaluate the long-term efficiency of the supercapacitors constructed as part of this research. The results are illustrated in Fig. 13.

The analysis of the supercapacitor performance relies on the specific capacity, which refers to the amount of energy a material can store per unit mass [70]. Fig. 13a depicts the specific capacity curves of the samples. These curves represent the capacity of the materials after the charge-discharge period, specifically at a current density of 0.1 A/g. The CF compound has the lowest specific capacity value among all SC designs. By substituting with Ni^{2+} ions, the specific capacity increases considerably, and the supercapacitor fabricated utilizing NF exhibits highly efficient capability for energy storage in terms of the specific capacity values.

Capacitance retention refers to measuring the extent to which a supercapacitor maintains its initial capacity after a certain number of charge and discharge periods. Evaluating the supercapacitor's long-term endurance and performance stability depends on an essential feature. A high value of capacitance retention signifies the supercapacitor's ability to maintain its capacitance consistently and reliably throughout an extended operational lifespan, enabling repeated usage [71]. The retention values of capacitance for Ni-Co ferrite nanoparticles after 5000 cycles are depicted in Fig. 13b.

Capacitance retention values for Co-ferrite and CF-20%Ni have continuously decline after 400 cycles. The increase in nickel content is associated with an enhancement in the capacitance retention values of the material. In the case of the supercapacitor prepared utilizing $NiFe_2O_4$, the capacitance retention reached its lowest point at 2000 cycles, after which the value of capacitance retention exhibited a rise. This observation implies that the $NiFe_2O_4$ sample has cyclic stability. Nevertheless, it has been shown that the supercapacitors fabricated utilizing samples containing Ni concentrations of up to 40 % have a capacitance retention value nearing 100 % after 5000 cycles, indicating that supercapacitors fabricated with specific nickel concentrations exhibit favorable characteristics for extended utilization periods. The GCPL analysis confirms the superior electrochemical performance of the Ni-substituted Co-ferrite nanoparticles. The CF-20%Ni sample exhibits the highest specific capacitance (208.1 F/g), energy density (7.23 Wh/kg), and power density (88.4 kW/kg), which can be attributed to its mesoporous structure, multiple redox pairs, and small crystallite size.

Based on the electrochemical results of the symmetrical supercapacitors developed using the samples presented above, the specific capacitance, energy density, and power density values are evaluated and the obtained values are presented in Table 5. The specific capacitance increased by Ni substitution compared with CF sample revealing an optimum substituting concentration. Hence, the CF-20%Ni sample performs best regarding specific capacitance, energy, and power density.

The enhancement in electrochemical characteristics of CF by substituting Co^{2+} with Ni^{2+} ions can be due to (i) the rearrangement of cations on octahedral sites observed in Raman spectra which can generates defects acting as additional ion diffusion pathways and electrochemical active sites [72,73] and, (ii) multiple metal cation valences,

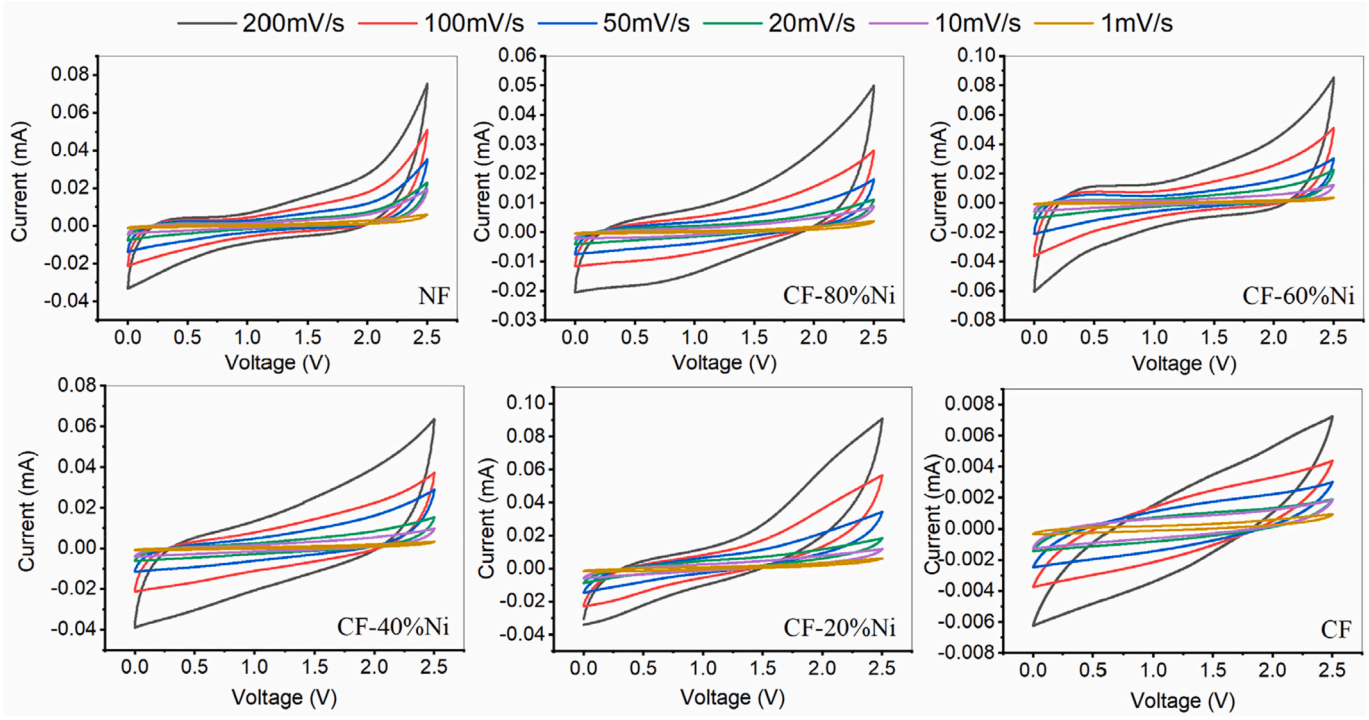


Fig. 11. CV profiles of the supercapacitors of two-electrode configuration with 1M LiPF6 electrolyte.

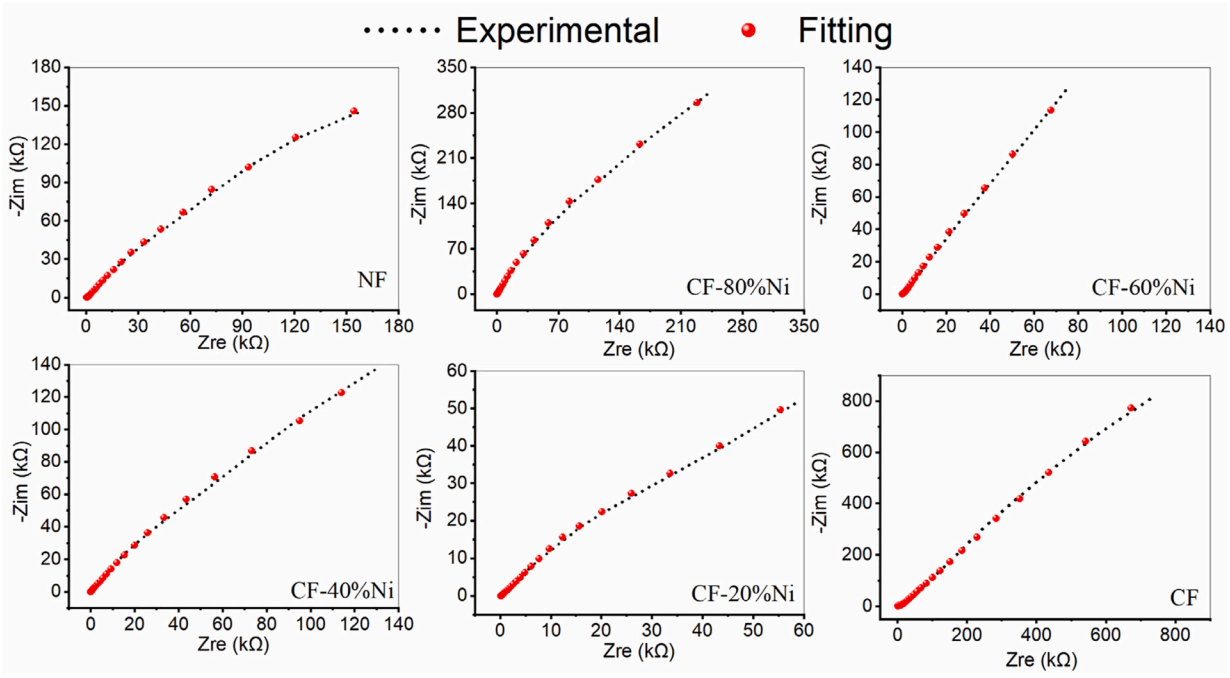


Fig. 12. The impedance data for all supercapacitors includes experimental and fitted values, Nyquist profiles, fitted equivalent circuit components, and the corresponding equivalent circuits.

Table 4
The parameters of the equivalent circuit fitting analysis.

Equivalent Circuit (R_1+Q_2/R_2+Q_3/R_3)						
	CF	CF-20% Ni	CF-40% Ni	CF-60% Ni	CF-80% Ni	NF
R_1	5.08	2.00	1.55	1.22	0.82	1.62
R_2	0.78 x10^{15}	0.29 x 10^5	3.87 x10^5	0.007 x 10^5	0.89 x 10^5	0.013 x 10^5
R_3	9072	0.13 x10^6	0.21 x10^6	11.75 x10^6	0.75 x10^6	3.38 x10^6
Q_2	4.5 x10^{-6}	97.6 x10^{-6}	12.9 x10^{-6}	15.8 x10^{-6}	42.4 x10^{-6}	68.7 x10^{-6}
Q_3	0.6 x10^{-6}	43.6 x10^{-6}	44.8 x10^{-6}	138 x10^{-6}	56.0 x10^{-6}	16.0 x10^{-6}
a_2	0.56	1.0	0.74	0.79	0. 76	0.62
a_3	0.57	0.77	1.0	0.78	1.0	0.81

*** The unit of R is ohm; Q is F. s^(a-1). "a" is a constant known as the ideality factor.

which are involved in complex redox reactions. Additionally, CF-20%Ni sample has the lowest band gap energy between Ni-substituted cobalt ferrite samples, facilitates faster charge transfer and favoring the specific capacitance [74].

To evidence the potential application of the synthesized materials as photocatalysts and supercapacitors, a comparison with the reported data in the literature concerning similar materials was done and are shown in Tables 6 and 7. In Table 6, the degradation efficiency of various substituted ferrites is presented. A comparison between the results is difficult to realize since several parameters influence the photocatalysis efficiency: pollutant type and concentration, photocatalyst concentration, irradiation time, irradiation source.

Regarding the supercapacitor applications, when compared to similar materials reported in the literature (Table 7), it is important to note that most studies use a 3-electrode system, while this work employs a 2-electrode real system. Despite this, the Ni-substituted Co-ferrite nanoparticles, particularly the CF-20%Ni sample, exhibit competitive performance in terms of specific capacitance, energy density, and power density. This highlights the potential of these materials for practical supercapacitor applications.

4. Conclusions

This paper reports a series of Co-ferrites substituted with Ni ions as bifunctional nanomaterial for photocatalysis and supercapacitor application. $Ni_xCo_{1-x}Fe_2O_4$ nanoparticles with various Ni content (x = 0, 0.2, 0.4, 0.6 08, 1) were synthesized by precipitation method. XRD diffraction patterns show that all the samples are crystalline having cubic symmetry without secondary phases. Substituting Co^{2+} with Ni^{2+} ions was proven by the variation in cell parameters, which decreased with the gradual replacement of Co^{2+} with Ni^{2+} due to the lower ionic radius of Ni^{2+} compared with Co^{2+} ions. Information about the position of Co and Ni ions in the lattice was obtained from Raman spectroscopy. Thus, analyzing the Raman spectra, results that Co^{2+} ion partially substitute Fe^{3+} ion in tetrahedral sites and the substitution with Ni^{2+} ions lead to a rearrangement of the cations in octahedral sites. From the TEM images, the morphology of the samples was evidenced, showing nanoparticles with spherical and rectangular shapes for all the samples, but with different average sizes from sample to sample, the size of the nanoparticles decreasing with the Ni content in following the XRD results. EPR spectroscopy shows that the samples are ferromagnetic at room temperature, so they could be manipulated easily in solution. The EPR spectrum at 250 K of CF-60%Ni clearly shows both ferrites' contribution, attesting the presence of both phases $NiFe_2O_4$ and $CoFe_2O_4$ in nanomaterial. The optical response in visible domain was proven by UV–Vis spectra. Using the absorption spectra, the band gap energy was evaluated and their value is increasing by substituting with Ni ions. Visible light photocatalytic performance was determined using RhB solution, and the results show there is an optimum amount of Ni ions leading to the best photocatalytic activity. The ROS species generated by the sample were evaluated from EPR coupled with the spin trapping technique, and this method demonstrated only the generation of superoxide radicals. The obtained results allowed the identification of photocatalytic mechanism. Additionally, the sample with the best photocatalytic performances was combined with PVDF membrane to increase its hydrophilicity and self-cleaning properties. The successful

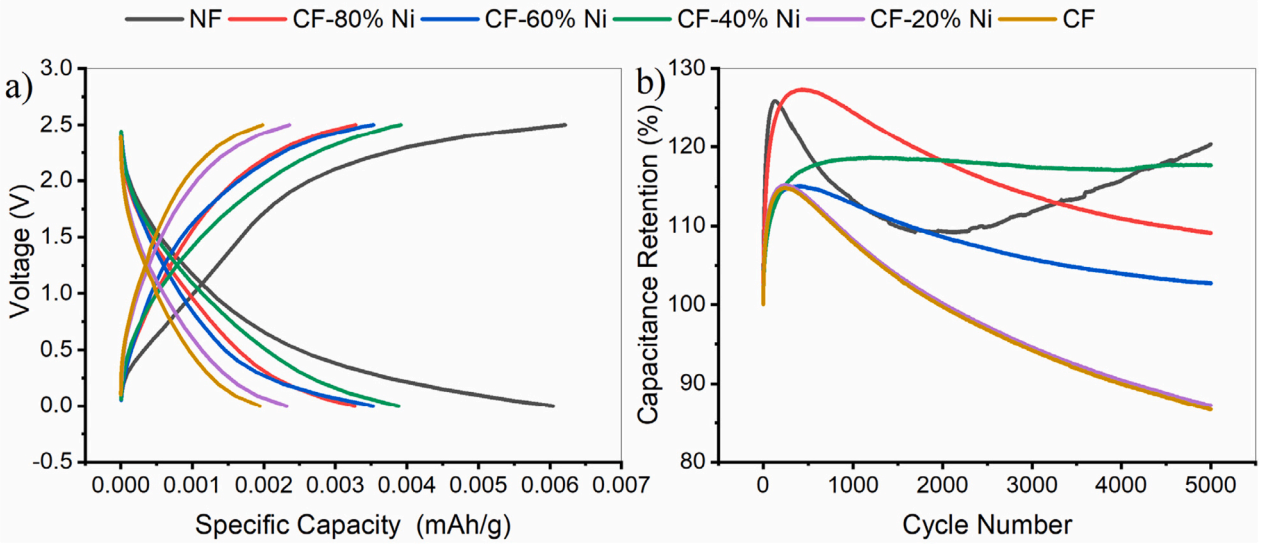


Fig. 13. Specific capacity curves of the samples (a). The retention values of capacitance for the samples after 5000 cycles (b).

Table 5
The electrochemical characteristics of the fabricated supercapacitors.

Sample	Specific Capacitance (F/g)	Energy Density (Wh/kg)	Power Density (kW/kg)
CF	53.3	1.85	31.5
CF-20% Ni	208.1	7.23	88.4
CF-40% Ni	142.7	4.95	37.3
CF-60% Ni	132.2	4.59	45.6
CF-80% Ni	109.1	3.79	40.5
NF	188.3	6.54	40.3

Table 6
Comparison of photocatalytic activity of various substituted ferrites.

Sample	Light	Pollutant	Irradiation time (min)	Photocat activity %	Ref.
$Mg_{1-x}Ni_xFe_2O_4$	visible	MB	300	85–95	[75]
$Mg_{0.5}Zn_{0.5}Co_xFe_2O_4$	sun	MB	160	65	[76]
$Ni_{0.5}Zn_{0.5}Fe_2O_4$	sun	fluorescein	60	88	[77]
$Nb_xCu_{1-x}Fe_2O_4$	UV	RhB	90	66	[78]
$Ni_xCo_{1-x}Fe_2O_4$	visible	RhB	300	81	this work

Table 7
Comparison of supercapacitor performances of various substituted ferrites.

Sample	C_S	E_D	P_D	Ref.
	F/g	Wh/kg	kW/kg	
$NiCoFe_2O_4$	50.0	4.79	1.4	[79]
$Ni_{0.4}Co_{0.6}Fe_2O_4$	237	10.3	4.2	[80]
$Zn_xNi_{1-x}Fe_2O_4$	581	8.85	1.15	[81]
$Ni_{0.25}Mg_{0.75}Fe_2O_4$	133.95	6.46	147.3	[82]
$NiCo_2S_4$	154.1	n.a.	n.a.	[83]
$CoFe_2O_4$	280	10	2.5	[84]
$NiCoFe_2O_4$	314.97	3.82	1.24	[85]
$NiFe_2O_4$	240.9	10.15	0.14	[86]
$Ni_{0.5}Zn_{0.5}Fe_2O_4$	151	17	0.45	[87]
$NiCoFe_2O_4$	43	6.4	1.90	[88]
$Ni_xCo_{1-x}Fe_2O_4$	208.1	7.23	88.4	this work

deposition on the nanoparticles on the membrane surface was proven by STEM and EDX investigations. Also, by UV–Vis absorption spectroscopy, the visible response of modified membrane was evidenced. Ni-Co ferrite nanoparticles were also studied as electrode materials in symmetrical supercapacitor devices. By substituting Co^{2+} with Ni^{2+} ions, the specific capacitance of cobalt ferrite increases from 53.3 to 208.1 F/g.

CRediT authorship contribution statement

Dana Toloman: Writing – original draft, Validation, Supervision, Methodology, Investigation, Conceptualization. **Maria Stefan:** Writing – original draft, Methodology, Investigation. **Cameliu Himcinschi:** Investigation. **Iolanda Ganea:** Investigation. **Lucian Barbu:** Investigation. **Arpad Rostas:** Investigation. **Ahmet Gungor:** Writing – original draft, Investigation. **Emre Erdem:** Writing – original draft, Validation, Supervision. **Adriana Popa:** Writing – original draft, Validation, Methodology, Investigation.

Data availability

Data will be made available on request.

Declaration of competing interest

The authors declare that they have no known competing financial interests or personal relationships that could have appeared to influence the work reported in this paper.

Acknowledgments

Acknowledgments Financial support was provided by a grant from the Ministry of Research, Innovation and Digitization, CNCS – UEFISCDI, project number PN-III-P1-1.1-TE-0836, within PNCDI III and from the MCID through the “Nucleu” Program within the National Plan for Research, Development and Innovation 2022–2027, project PN 23 24 01 03.

Appendix A. Supplementary data

Supplementary data to this article can be found online at https://doi.org/10.1016/j.ceramint.2025.01.543.

References

[1] S. Chu, A. Majumdar, Opportunities and challenges for a sustainable energy future, Nature 488 (2012) 294–303, https://doi.org/10.1038/nature11475.

[2] M. Zouhier, K. Tanji, J.A. Navio, M.C. Hidalgo, C. Jaramillo-Páez, A. Kherbeche, Preparation of $ZnFe_2O_4$/ZnO composite: effect of operational parameters for photocatalytic degradation of dyes under UV and visible illumination, J. Photochem. Photobiol., A: Chem 390 (2020) 112305, https://doi.org/10.1016/j.jphotochem.2019.112305.

[3] U. Shanker, M. Rani, V. Jassal, Degradation of hazardous organic dyes in water by nanomaterials, Environ. Chem. Lett. 15 (2017) 623–642, https://doi.org/10.1007/s10311-017-0650-2.

[4] F. Xiao, B. Liu, In-situ etching-induced self-assembly of metal clusters decorated one-dimensional semiconductor for solar-powered water splitting: unraveling cooperative synergy by photoelectrochemical investigations, Nanoscale 9 (2017) 17118–17132, https://doi.org/10.1039/C7NR06697J.

[5] P. Lianos, Production of electricity and hydrogen by photocatalytic degradation of organic wastes in a photoelectrochemical cell: the concept of the Photofuelcell: a review of a re-emerging research field, J. Hazard Mater. 185 (2011) 575–590, https://doi.org/10.1016/j.jhazmat.2010.10.083.

[6] D. Huang, X. Yan, M. Yan, G. Zeng, C. Zhou, J. Wan, M. Cheng, W. Xue, Graphitic carbon nitride-based heterojunction photoactive nanocomposites: applications and mechanism insight, ACS Appl. Mater. Interfaces 10 (2018) 21035–21055, https://doi.org/10.1021/acsami.8b03620.

[7] S. Sato, T. Arai, T. Morikawa, K. Uemura, T.M. Suzuki, H. Tanaka, T. Kajino, Selective CO2 conversion to formate conjugated with H2O oxidation utilizing semiconductor/complex hybrid photocatalysts, J. Am. Chem. Soc. 133 (2011) 15240–15243, https://doi.org/10.1021/ja204881d.

[8] M.A. Fox, M.T. Dulay, Heterogeneous photocatalysis, Chem. Rev. 93 (1993) 341–357, https://doi.org/10.1021/cr00017a016.

[9] D. Huang, Z. Li, G. Zeng, C. Zhou, W. Xue, X. Gong, X. Yan, S. Chen, W. Wang, M. Cheng, Megamerger in photocatalytic field: 2D g-C3N4 nanosheets serve as support of 0D nanomaterials for improving photocatalytic performance, Appl. Catal. B Environ. 240 (2019) 153–173, https://doi.org/10.1016/j.apcatb.2018.08.071.

[10] W. Xue, D. Huang, G. Zeng, J. Wan, M. Cheng, C. Zhang, C. Hu, J. Li, Performance and toxicity assessment of nanoscale zero valent iron particles in the remediation of contaminated soil: a review, Chemosphere 210 (2018) 1145–1156, https://doi.org/10.1016/j.chemosphere.2018.07.118.

[11] H.-Y. He, Y. Yan, J.-F. Huang, J. Lu, Rapid photodegradation of methyl blue on magnetic $Zn_{1-x}Co_xFe_2O_4$ nanoparticles synthesized by hydrothermal process, Sep. Purif. Technol. 136 (2014) 36–41, https://doi.org/10.1016/j.seppur.2014.08.028.

[12] P.N. Anantharamaiah, S. Mondal, K.S. Manasa, Sujoy Saha, Pai M. Maya, Enhancing the catalytic activity of recyclable nanocrystalline $NiFe_2O_4$ by replacing Ni by Cu, Ceram. Int. 46 (2020) 1220–1226, https://doi.org/10.1016/j.ceramint.2019.08.276.

[13] M. Srinivas, Preparation, characterization and photocatalytic activity of nickel substituted $CoFe_2O_4$: exploration of changes in the micro structural parameters and distribution of cations in the lattice, Mater. Res. Express 6 (2019) 1150f9, https://doi.org/10.1088/2053-1591/ab51af.

[14] M. Li, Y. Xiong, X. Liu, X. Bo, Y. Zhang, C. Han, L. Guo, Facile synthesis of electrospun MFe_2O_4 (M = Co, Ni, Cu, Mn) spinel nanofibers with excellent electrocatalytic properties for oxygen evolution and hydrogen peroxide reduction, Nanoscale 7 (2015) 8920–8930, https://doi.org/10.1039/C4NR07243J.

[15] M.N. Iliev, D. Mazumdar, J.X. Ma, A. Gupta, F. Rigato, J. Fontcuberta, Monitoring B-site ordering and strain relaxation in $NiFe_2O_4$ epitaxial films by polarized Raman spectroscopy, Phys. Rev. B 83 (2011) 014108, https://doi.org/10.1103/PhysRevB.83.014108.

[16] E. Erdem, Electron beam curing of $CoFe_2O_4$ nanoparticles, Hybrid. Mater. 1 (2014) 62–70, https://doi.org/10.2478/hyma-2014-0003.

[17] M.A. Almessiere, Y. Slimani, H. Güngüne, V.G. Kostishyn, S.V. Trukhanov, A. V. Trukhanov, A. Baykal, A. Impact of Eu3+ion substitution on structural, magnetic and microwave traits of Ni–Cu–Zn spinel ferrites, Ceram. Int. 46 (2020) 11124–11131, https://doi.org/10.1016/j.ceramint.2020.01.132.

[18] A. Lassoued, M. Lassoued, B. Dkhil, S. Ammar, A. Gadri, Synthesis, photoluminescence and Magnetic properties of iron oxide (α-Fe2O3) nanoparticles through precipitation or hydrothermal methods, Physica E 101 (2018) 29, https://doi.org/10.1016/j.physe.2018.04.009.

[19] M. Sukumar, J.R. Rajabathar, H. AL-Lohedan, S. Suresh, C.S. Dash, M. Sundararajan, P.S. Subudhi, S. Arokiyaraj, E. Yanmaz, S. Yuvaraj, R.S. Rimal Isaac, Synthesize and characterization of copper doped nickel ferrite nanoparticles effect on magnetic properties and visible light catalysis for rhodamine dye degradation mechanism, J. Alloy. Compd. 953 (2023) 169902, https://doi.org/10.1016/j.jallcom.2023.169902.

[20] A. Nadumane, K. Shetty, K.S. Anantharaju, H.P. Nagaswarupa, D. Rangappa, Y. S. Vidya, H. Nagabhushana, S.C. Prashantha, Sunlight photocatalytic performance of Mg-doped nickel ferrite synthesized by a green sol-gel route, J. Sci.: Adv. Mater. Devices. 4 (2019) 89–100, https://doi.org/10.1016/j.jsamd.2018.12.002.

[21] A. Lassoued, M.S. Lassoued, B. Dkhil, S. Ammar, A. Gadri, Substituted effect of Al3 + on structural, optical, magnetic and photocatalytic activity of Ni ferrites, J. Magn. Magn Mater. 476 (2019) 124–133, https://doi.org/10.1016/j.jmmm.2018.12.062.

[22] M. Dhiman, B. Chudasama, V. Kumar, K.B. Tikoo, S. Singhal, Augmenting the photocatalytic performance of cobalt ferrite via change in structural and optical properties with the introduction of different rare earth metal ions, Ceram. Int. 45 (2019) 3698–3709, https://doi.org/10.1016/j.ceramint.2018.11.033.

[23] M. Srinivas, Superior photocatalytic activity of Mn-doped $CoFe_2O_4$ under visible light irradiation: exploration of hopping and polaron formation in the spinel structure, Mater. Sci. Eng. B 270 (2021) 115222, https://doi.org/10.1016/j.mseb.2021.115222.

[24] N.B. Turan, S. Erkan, G.O. Engin, S. Bilgili, Nanoparticles in the aquatic environment: usage, properties, transformation and toxicity—a review, Process Saf. Environ. Prot. 130 (2019) 238–249, https://doi.org/10.1016/j.psep.2019.08.014.

[25] M. Romay, N. Diban, M.J. Rivero, A. Urtiaga, I. Ortiz, Critical issues and guidelines to improve the performance of photocatalytic polymeric membranes, Catalysts 10 (2020) 570, https://doi.org/10.3390/catal10050570.

[26] V. Vaiano, G. Iervolino, Facile method to immobilize ZnO particles on glass spheres for the photocatalytic treatment of tannery wastewater, J. Colloid Interf. Sci. 518 (2018) 192, https://doi.org/10.1016/j.jcis.2018.02.033.

[27] T.D. Kusworo, M. Yulfarida, A.C. Kumoro, S. Sumardiono, M. Djaeni, T. A. Kurniawan, M.H.D. Othman, B. Budiyono, A highly durable and hydrophilic PVDF- MoS2/WO3-PVA membrane with visible light driven self-cleaning performance for pollutant-burdened natural rubber wastewater treatment, J. Environ. Chem. Eng. 11 (2023) 109583, https://doi.org/10.1016/j.jece.2023.109583.

[28] A. Febriasari, I. Purnawan, M. Chalid, I. Ismojo, S. Kartohardjono, A direct comparison between poly(vinylidene) flouride and polysulfone flat sheet membrane; characterization and mechanical strength, IOP Conf. Ser. Earth Environ. Sci. 442 (2020) 012002, https://doi.org/10.1088/1755-1315/442/1/012002.

[29] S. Aani, C.J. Wright, N. Hilal, Investigation of UF membranes fouling and potentials as pre-treatment step in desalination and surface water applications, Desalination 432 (2018) 115–127, https://doi.org/10.1016/j.desal.2018.01.017.

[30] T.D. Kusworo, A.C. Kumoro, N. Aryanti, D.P. Utomo, H. Hasbullah, F.F. Lingga, A. Widiastuti, M. Yulfarida, F. Dalanta, T.A. Kurniawan. Simultaneous Photocatalytic and Membrane Filtration Using Graphene Oxide (GO)/SiO2 Composite for enhanced removal of Organic Pollutant and Ammonia from Natural Rubber-Laden Wastewater. SSRN Electron. J., https://doi.org/10.2139/ssrn.4017566.

[31] R. Li, Y. Ren, P. Zhao, J. Wang, J. Liu, Y. Zhang, Graphitic carbon nitride (g-C3N4) nanosheets functionalized composite membrane with self-cleaning and antibacterial performance, J. Hazard Mater. 365 (2019) 606–614, https://doi.org/10.1016/j.jhazmat.2018.11.033.

[32] A.N. Alqarni, E. Cevik, M.A. Almessiere, A. Baykal, M.A. Gondal, M. Hassan, A. Bozkurt, A. Iqbal, S.M. Asiri, Y. Slimani, Fabrication of Bismuth-doped Co–Ni spinel ferrite electrodes for enhanced cyclic performance in asymmetric supercapacitors, J. Phys. Chem. Solids 177 (2023) 111288, https://doi.org/10.1016/j.jpcs.2023.111288.

[33] V.V. Jadhav, R.S. Mane, P.V. Shinde, Bismuth-ferrite-based electrochemical supercapacitors, part of the book series, Springer Briefs in Materials (2020), https://doi.org/10.1007/978-3-030-16718-9.

[34] S. Khalid, C. Cao, Ahmad Aziz, L. Wang, M. Tanveer, I. Aslam, M. Tahir, F. Idrees, Y. Zhu, Microwave assisted synthesis of mesoporous NiCo2O4 nanosheets as electrode material for advanced flexible supercapacitors, RSC Adv. 5 (2015) 33146–33154, https://doi.org/10.1039/C5RA02180D.

[35] S. Meena, K.S. Anantharaju, S. Malini, A. Dey, L. Renuka, S.C. Prashantha, Y. S. Vidya, Impact of temperature-induced oxygen vacancies in polyhedron MnFe2O4 nanoparticles: as excellent electrochemical sensor, supercapacitor and active photocatalyst, Ceram. Int. 47 (2021) 14723–14740, https://doi.org/10.1016/j.ceramint.2020.12.217.

[36] A. Kumar, B.N. Mahanty, A. Rawat, R. Muhammad, R.K. Panigrahi, D. Pradhan, P. Mohanty, Transition-metal-substituted nanoporous manganese ferrites Mn0.95M0.05Fe2O4 (M: Co, Cu, and Zn) as electrode materials for high-performance supercapacitors in redox-active nonaqueous electrolytes, Energy Fuels 37 (2023) 6810–6823, https://doi.org/10.1021/acs.energyfuels.3c00281.

[37] A. Manohar, V. Vijayakanth, S.V.P. Vattikuti, K.H. Kim, Synthesis and characterization of Mg^{2+} substituted $MnFe_2O_4$ nanoparticles for supercapacitor applications, Ceram. Int. 48 (2022) 30695–30703, https://doi.org/10.1016/j.ceramint.2022.07.018.

[38] S. Divya, P. Sivaprakash, S. Raja, S. Esakki Muthu, Ikhyun Kim, N. Renuka, S. Arumugam, Tae Hwan Oh, Impact of Zn doping on the dielectric and magnetic properties of $CoFe_2O_4$ nanoparticles, Ceram. Int. 48 (2022) 33208–33218, https://doi.org/10.1016/j.ceramint.2022.07.263.

[39] A. Ashfaq, M. Ghulam, M. Umair Subhani, H. Gulzar, I.G. Ahmad, A. Hafeez, A detailed investigation of lanthanum substituted bismuth ferrite for enhanced structural, optical, dielectric, magnetic and ferroelectric properties, Results Phys. 38 (2022) 105584, https://doi.org/10.1016/j.rinp.2022.105584.

[40] J. Suresh, B. Trinadh, B.V. Babu, P.V.S.S.S.N. Reddy, B.S. Mohan, A.R. Krishna, K. Samatha, Evaluation of micro-structural and magnetic properties of nickel nano-ferrite and Mn2+ substituted nickel nano-ferrite, Physica B 620 (2021) 413264, https://doi.org/10.1016/j.physb.2021.413264.

[41] V.G. Ivanov, M.V. Abrashev, M.N. Iliev, M.M. Gospodinov, J. Meen, M.I. Aroyo, Short-range B-site ordering in the inverse spinel ferrite NiFe2O4, Phys. Rev. B 82 (2010) 024104, https://doi.org/10.1103/PhysRevB.82.024104.

[42] P.R. Graves, C. Johnston, J.J. Campaniello, Raman scattering in spinel structure ferrites, Mater. Res. Bull. 23 (1988) 1651–1660, https://doi.org/10.1016/0025-5408(88)90255-3.

[43] C. Himcinschi, I. Vrejoiu, G. Salvan, M. Fronk, A. Talkenberger, D.R.T. Zahn, D. Rafaja, J. Kortus, Optical and magneto-optical study of nickel and cobalt ferrite epitaxial thin films and submicron structures, J. Appl. Phys. 113 (2013) 084101, https://doi.org/10.1063/1.4792749.

[44] R. Chen, W. Wang, X. Zhao, Y. Zhang, S. Wu, F. Li, Rapid hydrothermal synthesis of magnetic CoxNi1−xFe2O4 nanoparticles and their application on removal of Congo red, Chem. Eng. J. 242 (2014) 226–233, https://doi.org/10.1016/j.cej.2013.12.016.
[45] F. Nakagomi, S. da Silva, V.K. Garg, A.C. Oliveira, P.C. Morais, A. Franco, Influence of the Mg-content on the cation distribution in cubic $Mg_xFe_{3-x}O_4$ nanoparticles, J. Solid State Chem. 182 (2009) 2423–2429, https://doi.org/10.1016/j.jssc.2009.06.036.
[46] D. Rajan Babu, K. Venkatesan, Synthesis of nanophasic CoFe2O4 powder by self-igniting solution combustion method using mix up fuels, J. Cryst. Growth 468 (2017) 179–184, https://doi.org/10.1016/j.jcrysgro.2016.11.054.
[47] M. N. Iliev, D. Mazumdar, J. X. Ma, A. Gupta, F. Rigato, J. Fontcuberta, Monitoring B-site ordering and strain relaxation in NiFe2O4 epitaxial films by polarized Raman spectroscopy, Phys. Rev. B 83 (201) 014108, https://doi.org/10.1103/PhysRevB.83.014108.
[48] R. Topkaya, Ö. Akman, S. Kazan, B. Aktaş, Z. Durmus, A. Baykal, Surface spin disorder and spin-glass-like behaviour in manganese-substituted cobalt ferrite nanoparticles, J. Nanopart. Res. 14 (2012) 1156, https://doi.org/10.1007/s11051-012-1156-2.
[49] Y. Sánchez, S. Briceño, J. Larionova, J. Long, Y. Guari, P. Silva, Temperature dependence of the ferromagnetic resonance (FMR) for $Mn_xCo_{1-x}Fe_2O_4$ ($0 \leq x \leq 1$) nanoparticles, J. Mater. Res. 36 (2021) 3329–3338, https://doi.org/10.1557/s43578-021-00345-9.
[50] O. Pana, A. Petran, A. Popa, M. Stefan, T.D. Silipas, C. Leostean, B.S. Vasile, F. Pogacean, D. Toloman, $Zn_xFe_{3-x}O_4$–ZnO heterojunction interfaced with poly(L-DOPA) electron transfer mediator layer for enhanced visible light photocatalytic activity, J. Alloy. Compd. 986 (2024) 174168, https://doi.org/10.1016/j.jallcom.2024.174168.
[51] E.L. Verde, G.T. Landi, M.S. Carrião, A.L. Drummond, J.A. Gomes, E.D. Vieira, M. H. Sousa, A.F. Bakuzis, Field dependent transition to the non-linear regime in magnetic hyperthermia experiments: comparison between maghemite, copper, zinc, nickel and cobalt ferrite nanoparticles of similar sizes, AIP Adv. 2 (2012) 032120, https://doi.org/10.1063/1.4739533.
[52] G. Alvarez, H. Montiel, J.F. Barron, M.P. Gutierrez, R. Zamorano, Yafet–Kittel-type magnetic ordering in Ni0.35Zn0.65Fe2O4 ferrite detected by magnetosensitive microwave absorption measurements, J. Magn. Magn Mater. 322 (2010) 348–352, https://doi.org/10.1016/j.jmmm.2009.09.056.
[53] T. Peng, X. Zhang, H. Lv, L. Zan, Preparation of NiFe2O4 nanoparticles and its visible-light-driven photoactivity for hydrogen production, Catal. Commun. 28 (2012) 116–119, https://doi.org/10.1016/j.catcom.2012.08.031.
[54] M.P. Ghosh, S. Mukherjee, Size variation in nanocrystalline Zn0.2Ni0.8Gd0.05Fe1.95O4 ferrites: exchange bias effect and its correlation with disordered surface spins, Mater. Res. Bul. 125 (2020) 110785, https://doi.org/10.1016/j.materresbull.2020.110785.
[55] D. Toloman, A. Mesaros, A. Popa, T.D. Silipas, S. Neamtu, G. Katona, V-doped ZnO particles: synthesis, structural, optical and photocatalytic properties, J. Mater. Sci. Mater. Electron. 27 (2016) 5691–5698, https://doi.org/10.1007/s10854-016-4480-y.
[56] B.S. Holinsworth, D. Mazumdar, H. Sims, Q.-C. Sun, M.K. Yurtisigi, S.K. Sarker, A. Gupta, W.H. Butler, J.L. Musfeldt, Chemical tuning of the optical band gap in spinel ferrites: CoFe2O4 vs NiFe2O4, Appl. Phys. Lett. 103 (2013) 082406, https://doi.org/10.1063/1.4818315.
[57] S. Joshi, M. Kumar, Effect of Ni^{2+} substitution on structural, magnetic, dielectric and optical properties of mixed spinel CoFe2O4 nanoparticles, Ceram. Int. 42 (2016) 18154–18165, https://doi.org/10.1016/j.ceramint.2016.08.130.
[58] J.L. Clement, N. Ferre, D. Siri, H. Karoui, A. Rockenbauer, P. Tordo, Assignment of the EPR spectrum of 5,5-Dimethyl-1-pyrroline N-oxide (DMPO) superoxide spin adduct, J. Org. Chem. 70 (2005) 1198–1203, https://doi.org/10.1021/jo048518z.
[59] R. Zhang, C. Zhao, J. Yu, Z. Chen, J. Jiang, K. Zeng, L. Cai, Z. Yang, Synthesis of dual Z-scheme photocatalyst ZnFe2O4/PANI/Ag2CO3 with enhanced visible light photocatalytic activity and degradation of pollutants, Adv. Powder Technol. 33 (2022) 103348, https://doi.org/10.1016/j.apt.2021.10.040.
[60] S. Meena, K.S. Anantharaju, Y.S. Vidya, L. Renuka, B. Uma, S.C. Sharma, B. Daruka Prasad, Sunil S. More, Enhanced sunlight driven photocatalytic activity and electrochemical sensing properties of Ce-doped MnFe2O4 nano magnetic ferrites, Ceramics Int 47 (2021) 14760–14774, https://doi.org/10.1016/j.ceramint.2020.11.105.
[61] E. Pervaiz, M.S.A. Virk, A.K. Tareen, B. Zhang, Q. Zhao, Z. Wang, M. Yang, Magnetic micro scavengers: highly porous $Ni_{1-x}Co_xFe_2O_4$ microcubes for efficient disintegration of nitrophenol, Nanotechnology 29 (2018) 215710, https://doi.org/10.1088/1361-6528/aab4c8.
[62] T. Shen, L. Zhong, X. Liu, J. Zhang, D. Zhang, K. He, C. Yuan, Y. Xu, L. Dai, Decorating Au nanoparticles onto optimized P(tBA-co-DMAEMA) carriers for ameliorative catalytic capability, J. Appl. Polym. Sci. 137 (2020) 48920, https://doi.org/10.1002/app.48920.
[63] A. Hroub, M. Hasan Aleinawi, M. Stefan, M. Mihet, A. Ciorita, F. Bakan-Misirlioglu, E. Erdem, A. Mihai Rostas, Vanadium-doped magnesium oxide nanoparticles as electrodes in supercapacitor devices, J. Alloys Comp. 958 (2023) 170442, https://doi.org/10.1016/j.jallcom.2023.170442.
[64] D.K. Narale, P.D. Kumbhar, R.R. Bhosale, R.C. Ghaware, K.D. Patil, J.H. Kim, S. S. Kolekar, Rational design of binder free $NiFe_2O_4$@$CoFe_2O_4$ core–shell nanoflake arrays synthesized by chemical bath deposition for supercapacitor application, J. Energy Storage 66 (2023) 107477, https://doi.org/10.1016/J.EST.2023.107477.
[65] S.B. Aziz, R.T. Abdulwahid, M.H. Hamsan, M.A. Brza, R.M. Abdullah, M.F. Kadir, S. K. Muzakir, Structural, impedance, and EDLC characteristics of proton conducting chitosan-based polymer blend electrolytes with high electrochemical stability, Molecules 24 (2019) 3508, https://doi.org/10.3390/MOLECULES24193508.
[66] H. Wang, L. Pilon, Physical interpretation of cyclic voltammetry for measuring electric double layer capacitance, Electrochim. Acta 64 (2012) 130–139, https://doi.org/10.1016/j.electacta.2011.12.118.
[67] V. Vivier, M. Orazem, Impedance analysis of electrochemical systems, Chem. Rev. 122 (2022) 11131–11168, https://doi.org/10.1021/acs.chemrev.1c00876.
[68] D. Qu, G. Wang, J. Kafle, J. Harris, L. Crain, Z. Jin, D. Zheng D. Qu, G. Wang, J. Kafle, J. Harris, L. Crain, D. Zheng, Z. Jin, Electrochemical impedance and its applications in energy-storage systems, Small Methods 2 (8) (2018) 1700342, https://doi.org/10.1002/SMTD.201700342.
[69] A.Ch Lazanas, M.I. Prodromidis, Electrochemical impedance Spectroscopy—A tutorial, ACS Meas. Sci. Au 3 (2023) 162–193, https://doi.org/10.1021/acsmeasuresciau.2c00070.
[70] J. Liu, J. Wang, C. Xu, H. Jiang, C. Li, L. Zhang, J. Lin, Z.X. Shen, Advanced energy storage devices: basic principles, analytical methods, and rational materials design, Adv. Sci. 5 (2018) 1700322, https://doi.org/10.1002/ADVS.201700322.
[71] M. Weiss, R. Ruess, J. Kasnatscheew, Y. Levartovsky, N.R. Levy, P. Minnmann, L. Stolz, T. Waldmann, M. Wohlfahrt-Mehrens, D. Aurbach, M. Winter, Y. Ein-Eli, J. Janek, Fast charging of lithium-ion batteries: a review of materials aspects, Adv. Energy Mater. 11 (2021) 2101126, https://doi.org/10.1002/AENM.202101126.
[72] K. Malaie, M.R. Ganja, Spinel nano-ferrites for aqueous supercapacitors; linking abundant resources and low-cost processes for sustainable energy storage, J. Energy Storage 33 (2021) 102097, https://doi.org/10.1016/j.est.2020.102097.
[73] G. Nabi, W. Raza, M.A. Kamran, T. Alharbi, M. Rafique, M. Bilal Tahir, S. Hussain, N.R. Khalid, Q. Aain, N. Malik, R.S. Ahmed, C.B. Cao, Role of cerium-doping in CoFe2O4 electrodes for high performance supercapacitors, J. Energy Storage 29 (2020) 101452, https://doi.org/10.1016/j.est.2020.101452.
[74] S. Sharifi, A. Yazdani, K. Rahimi, Incremental substitution of Ni with Mn in $NiFe_2O_4$ to largely enhance its supercapacitance properties, Sci. Rep. 10 (2020) 10916, https://doi.org/10.1038/s41598-020-67802-z.
[75] A. Manohar, V. Vijayakanth, M.R. Pallavolu, K.H. Kim, Effects of Ni - substitution on structural, magnetic hyperthermia, photocatalytic and cytotoxicity study of $MgFe_2O_4$ nanoparticles, J. Alloy Compd. 879 (2021) 160515, https://doi.org/10.1016/j.jallcom.2021.160515.
[76] A. Irshad, M. Zulfiqar, H.M. Ali, N. Shahzadi, H.H.A. Gawad, C. Chokejaroenrat, C. Sakulthaew, F. Anjum, M. Suleman, Co-substituted Mg–Zn spinel nanocrystalline ferrites: synthesis, characterization and evaluation of catalytic degradation efficiency for colored and colorless compounds, Ceramics Int 48 (2022) 29805–29815, https://doi.org/10.1016/j.ceramint.2022.06.241.
[77] O.K. Nimisha, M. Akshay, S. Mannya, A.P. Reena Mary, Synthesis and photocatalytic activity of nickel doped zinc ferrite, Mater. Today Proc. 66 (2022) 2370–2373, https://doi.org/10.1016/j.matpr.2022.06.332.
[78] K. Gurushantha, B.N. Swetha, Sampath Chinnam, K. Keshavamurthy, S. Meena, B. S. Surendra, S. Malini, K.P. Roopa, Structural, Optical, Photocatalytic, and antimicrobial attributes of niobium substituted copper nanoferrites, Inorg. Chem. Commun. 156 (2023) 111162, https://doi.org/10.1016/j.inoche.2023.111162.
[79] B. Bhujun, M.T.T. Tan, A.S. Shanmugam, Study of mixed ternary transition metal ferrites as potential electrodes for supercapacitor applications, Results Phys. 7 (2017) 345–353, https://doi.org/10.1016/j.rinp.2016.04.010.
[80] N. Masanje Malima, M.D. Khan, J. Choi, R.K. Gupta, P. Mashazi, T. Nyokong, N. Revaprasadu, Solvent less synthesis of nanospinel $Ni_{1-x}Co_xFe_2O_4$ ($0 \leq x \leq 1$) solid solutions for efficient electrochemical water splitting and supercapacitance, RSC Adv. 11 (2021) 31002–31014, https://doi.org/10.1039/D1RA04833C.
[81] B. Dey, C. Manoharan, M. Venkateshwarlu, C.S. Pawar, S. Sagadevan, Exploring the effect of zinc substitution in nanocrystalline nickel ferrite for enhanced supercapacitor and gas sensing applications, Ceramics Int 50 (2024) 12121–12135, https://doi.org/10.1016/j.ceramint.2024.01.116.
[82] U. Wongpratat, P. Tipsawat, J. Khajonrit, E. Swatsitang, S. Maensiri, Effects of Nickel and Magnesium on electrochemical performances of partial substitution in spinel ferrite, J. Alloys Comp. 831 (2020) 154718, https://doi.org/10.1016/j.jallcom.2020.154718.
[83] D.K. Kulurumotlakatla, A.K. Yedluri, H.-Je Kim, Hierarchical $NiCo_2S_4$ nanostructure as highly efficient electrode material for high-performance supercapacitor applications, J. Energy Storage 31 (2020) 101619, https://doi.org/10.1016/j.est.2020.101619.
[84] M. Malarvizhi, S. Meyvel, M. Sandhiya, M. Sathish, M. Dakshana, P. Sathya, D. Thillaikkarasi, S. Karthikeyan, Design and fabrication of cobalt and nickel ferrites based flexible electrodes for high-performance energy storage applications, Inorg. Chem. Commun. 123 (2021) 108344, https://doi.org/10.1016/j.inoche.2020.108344.
[85] S. Nayak, S.S. Nayak, A.A. Kittur, S. Nayak, D.R. Joshi, Synthesis, fabrication, and performance evaluation of lanthanum doped nickel cobalt ferrite electrode for supercapacitors in energy storage applications, J. Energy Storage 101 (2024) 113918, https://doi.org/10.1016/j.est.2024.113918.
[86] X. Gao, W. Wang, J. Bi, Y. Chen, X. Hao, X. Sun, J. Zhang, Morphology-controllable preparation of $NiFe_2O_4$ as hig performance electrode material for supercapacitor, Electrochim. Acta 296 (2019) 181–189, https://doi.org/10.1016/j.electacta.2018.11.054.
[87] B. Nawaz, G. Ali, M.O. Ullah, S. Rehman, F. Abbas, Investigation of the electrochemical properties of $Ni_{0.5}Zn_{0.5}Fe_2O_4$ as binder-based and binder-free electrodes of supercapacitors, Energies 14 (2021) 3297, https://doi.org/10.3390/en14113297.
[88] M. Mayakkannan, A. Murugan, A. Shameem, V. Siva, S. Sasikumar, S. Thangarasu, S. Asath Bahadur, Investigations on ternary transition metal ferrite: NiCoFe2O4 as

potential electrode for supercapacitor prepared by microwave irradiation method, J. Energy Storage 44 (2021) 103257, https://doi.org/10.1016/j.est.2021.103257.